MULTISCALE MODEL. SIMUL.
Vol. 5, No. 4, pp. 1087–1127

A FRAMEWORK FOR MODELING SUBGRID EFFECTS FOR TWO-PHASE FLOWS IN POROUS MEDIA*

THOMAS Y. HOU†, ANDREW WESTHEAD†, AND DANPING YANG‡

Abstract. In this paper, we study upscaling for two-phase flows in strongly heterogeneous porous media. Upscaling a hyperbolic convection equation is known to be very difficult due to the presence of nonlocal memory effects. Even for a linear hyperbolic equation with a shear velocity field, the upscaled equation involves a nonlocal history dependent diffusion term, which is not amenable to computation. By performing a systematic multiscale analysis, we derive coupled equations for the average and the fluctuations for the two-phase flow. The homogenized equations for the coupled system are obtained by projecting the fluctuations onto a suitable subspace. This projection corresponds exactly to averaging along streamlines of the flow. Convergence of the multiscale analysis is verified numerically. Moreover, we show how to apply this multiscale analysis to upscale two-phase flows in practical applications.

Key words. porous media, upscaling, homogenization, hyperbolic, numerical modeling

AMS subject classifications. Primary, 76S05, 76M50; Secondary, 35M10

DOI. 10.1137/050646020

1. Introduction.

The understanding and modeling of flow through porous media is an important issue in several branches of engineering. In petroleum engineering, for instance, if one wishes to model the process, water is injected into an oil-saturated porous media in an attempt to displace the oil so that it can be collected. In groundwater contaminant studies the transport of dissolved material, such as toxic metals or radioactive waste, and how it affects drinking water supplies, is of interest.

Modeling such flows is difficult, and a principal source of the difficulty is the presence of widely different length scales in the problems. In modeling an oil reservoir, for example, geological data will be gathered over an area extending hundreds of meters, if not kilometers. Large-scale geological features will be present, such as "faults" as well as very small scale features such as layers created by sedimentation. When using traditional numerical methods we need to use spatial discretizations that are capable of resolving all these length scales. Even with improving computer technologies this is a formidable task for most data sets, both in terms of memory and computational time. However, for the most part, the resolution required for the smallest scale is greater than that needed for engineering purposes. Average properties of the flow, such as the total amount of oil produced, are often of more importance.

To address both these issues, various "upscaling" schemes have been proposed. In an upscaling scheme, one solves only for the average flow features, and the effect of the small-scale features is modeled. Since capturing average quantities requires

*Received by the editors November 24, 2005; accepted for publication (in revised form) June 30, 2006; published electronically December 5, 2006.
http://www.siam.org/journals/mms/5-4/64602.html

†Applied and Computational Mathematics, 217-50, Caltech, Pasadena, CA 91125 (hou@acm.caltech.edu, andrew.westhead@lehman.com). The first author's research was in part supported by NSF ITR grant ACI-0204932 and NSF FRG grant DMS-0353838.

‡School of Mathematics and System Science, Shandong University, Jinan, Shandong 250100, China (dpyang@sdu.edu.cn). This author's research was supported in part by the National Basic Research Program of China under grant 2005CB321703, by the NSFC under grants 10571108 and 10441005, and by the Research Fund for Doctoral Program of High Education of the Education Ministry of China under grant 2005042203.

less grid resolution, the schemes should use less computer memory and CPU time. The goal of research in this area is to make practical simulations available on limited computer resources. However, the existing upscaling methods often have limitations. Most methods do not have a very firm mathematical basis, and some rely heavily on experience. Other methods make very restrictive assumptions on the nature of the small scale features and are therefore applicable only in a limited range of data sets. A common assumption is that the effect of the small-scale features on the flow is small, which often does not hold.

The purpose of this study is to develop a systematic framework for developing upscaling schemes. We take a particular, simplified model for the porous media flow problem, which is given in section 2. This model retains the essential difficulty of the problem, namely the presence of multiple scales, and moreover, it is one that is used practically. The model consists of an elliptic equation for the fluid pressure and velocity field, and a nonlinear hyperbolic transport equation for the oil saturation in the porous media. Upscaling a hyperbolic convection equation is known to be very difficult due to the presence of nonlocal memory effect [26]. Even for a linear hyperbolic equation with a shear velocity field, the upscaled equation involves a nonlocal history dependent diffusion term, which is not amenable to computation. We remark that homogenization of transport equations has been studied before; see, e.g., [26, 24, 17, 9].

In this paper, we derive a homogenized equation for the hyperbolic saturation equation and develop an upscaling method for the two-phase flow in heterogeneous porous media. We perform a multiscale analysis by introducing a small length scale ϵ and small-scale variable $y = x/\epsilon$, where x is the large-scale variable. To facilitate the initial analysis we assume that there exist only these two length scales and that all functions of y are periodic, i.e., that the small-scale features are periodic. The multiscale analysis for the elliptic pressure equation is known. The multiscale analysis for the hyperbolic transport part is a new result, and this, along with the numerical results, is the main contribution of this work. We perform a multiscale analysis to derive coupled equations for the average and the fluctuations. The homogenized equations for the coupled system are obtained by projecting the fluctuations onto a suitable subspace. It turns out that this projection corresponds exactly to averaging along streamlines of the flow. In this subspace, the system becomes closed.

Once these multiscale equations have been derived, we consider the numerical implementation in section 4. We develop a novel approach to sampling the fluctuations in order to compute the small-scale large-scale interaction terms. We first discretize at the coarse level, using a sufficient number of grid points to resolve average features. Then, within each grid block we solve the equations for the fluctuations at a set number of points. These fluctuations are then used for computing the interaction terms. The resulting system for the transport part is a coupled hyperbolic system of equations with source terms. In order to solve the pressure equation on such a grid configuration, we make use of a variant of the multiscale finite element method developed by Hou and Wu [15]. It turns out that this complements perfectly the scheme for the transport part.

The numerical method for the hyperbolic part is then tested using a prescribed velocity field, and we demonstrate that the average is computed with first-order accuracy. Similarly, we demonstrate the efficacy of the multiscale finite element method (MsFEM) in capturing the velocity field. We then test the method for the case where the geological data (the permeability) is of the form described above, i.e., with small-scale features that are periodic. The results demonstrate that the method captures the average with first-order accuracy.

A method for extending the results to the case where permeability does not have scale separation is then described. We then use this in demonstrating that our method is applicable for practical examples. We present a number of numerical experiments in section 5 and compare the resulting solutions with those obtained by averaging resolved simulations. Our method captures this average very well.

The rest of the paper is organized as follows. In section 2, we describe the two-phase flow model. In section 3, we present our multiscale analysis for the two-phase flow equations. The numerical implementation issues and convergence study will be discussed in section 4, and numerical results with realistic data will be presented in section 5.

2. Modeling two-phase flows. In porous media flow simulation, we are interested in modeling the displacement, within a porous medium, of either oil, water, or some gas. In this paper, we will mainly look at the case of water-oil simulations. By porous media, we mean a solid with many small voids, or *pores*, which are connected and through which fluid may flow. The volume fraction of the pores as a total of the whole volume is known as the porosity. Since it is typical to view the pores as a microscale feature, this porosity is a macroscale feature, given pointwise. We usually consider one of the fluids to be displacing the other, as in the case of a oil-water flow where the water is pumped in so as to displace the oil. While the displacing fluid may be immiscible with the fluid being displaced, the displacement does not take place as with a sharp interface between the two fluids. Rather, simultaneous flow of the immiscible fluids takes place within the porous media.

In considering this simultaneous flow we assume, for the present, no mass transfer between the fluids. Mass transfer could potentially occur if there was a chemical reaction taking place between the fluids. Typically, one of the fluids *wets* the porous media more than the other; we refer to this as the wetting phase fluid (and identify it using the subscript w), and we refer to the other as the nonwetting phase fluid (and use the subscript n). Wettability describes the relative preference of a rock (from which the porous media is formed) to be covered by a certain phase. In a water-oil system, water is most often the wetting phase; in a oil-gas system, oil is the wetting phase. The saturation, S_k, of a phase k ($k = w, n$) is defined as the fraction of the void volume of the porous medium filled by that phase. Since the two fluids jointly fill the void space, we have

$$S_n + S_w = 1. \tag{1}$$

In order to model flows in porous media, it is vital to be able to model the velocity field. It is standard to use Darcy's law as the model for this [25]. For a single phase of fluid in the porous media, Darcy's law relates the fluid velocity $\boldsymbol{v}$ to the pressure p, viscosity μ, density ρ, and permeability K via

$$\boldsymbol{v} = -\frac{K}{\mu}\nabla p. \tag{2}$$

We take this law as an empirical fact [25]. Darcy's law can be thought of a viscous limit of the Navier–Stokes equation, which of course makes sense given how slowly fluid can flow within the porous media. In this equation, we have the permeability which, along with the porosity, is a basic property which characterizes the ease by which fluid can flow in the media. Low permeability characterizes regions where fluid cannot easily penetrate and high permeability where fluid can penetrate.

2.1. Simplified model problem. To make definite our mathematical formulation we simplify the model with the following assumptions: the porosity ϕ is constant throughout the media; the effects of compressibility can be ignored; capillary effects can be ignored; and gravitational effects can be ignored. In this case, the governing equations for pressure and saturation become, respectively [25],

$$\nabla \cdot (\lambda(S) K \nabla p) = 0, \tag{3}$$

$$\frac{\partial S}{\partial t} + \nabla \cdot (\boldsymbol{v} f(S)) = 0, \tag{4}$$

where $\boldsymbol{v} = -\lambda(S) K \nabla p$ is the total velocity, λ is the total mobility, and S is the saturation of the wetting phase. Henceforth, we will refer to these equations as the pressure equation and the saturation equation, respectively. The saturation equation (4) was first derived by Buckley and Leverett [4] and is therefore often referred to as the "Buckley–Leverett" equation. In order to complete the description of the model problem we must provide the forms for the functions λ and f in (3) and (4) and also provide appropriate initial and boundary conditions for the problem. The form of λ and f would in general be determined by experiment. However, for two-phase flow, a good model for $\lambda(S)$ and $f(S)$ is given by

$$\lambda(S) = S^2 + m(1-S)^2, \tag{5}$$

$$f(S) = \frac{S^2}{S^2 + m(1-S)^2}. \tag{6}$$

This model is widely used. Here m is the *mobility ratio*, which is a number between 0 and 1 that indicates the relative ease by which the nonwetting phase can flow. Often m will be less than 1, since oil does not flow as easily as water within the porous medium. We take $m = 1$ for all the computations in this paper.

The special case of single phase, or "tracer" flow, can be derived more easily and described in the same framework. The analysis gives us [25]

$$\lambda(S) = 1, \qquad f(S) = S. \tag{7}$$

One-phase flow is a useful model for the case of solute transport in groundwater flows. In this case contaminated and uncontaminated water, say, will be the two "phases" within the porous media. We now wish to solve the problem (3) and (4) for the evolution of the saturation. In general the permeability will be given as input data, and this is gathered using some geological survey or seismic imaging. Therefore, we will have to solve the system numerically.

In addition to the variation of the solution $S(x_1, x_2, t)$ with space and time, measures of the overall reservoir performance are usually calculated as well. An important characteristic is the so-called *fractional flow* which measures the fraction of oil produced at the production well with time. This is most easily computed in the case of the core-plug model, which will be described in the section on numerical results. In that case, the fractional flow is defined as

$$\Psi(t) = 1 - \frac{\int_0^1 f(S(1, x_2, t)) \boldsymbol{n} \cdot \boldsymbol{v}(1, x_2, t) dx_2}{\int_0^1 \boldsymbol{n} \cdot \boldsymbol{v}(1, x_2, t) dx_2}, \tag{8}$$

where $\boldsymbol{n} = (1, 0)$ is the outward pointing normal at the edge $x_1 = 1$. At $t = 0$ we have $\Psi = 1$, since initially the domain is oil saturated. After some time, however, we will

have $\Psi < 1$. This time is the *breakthrough time* corresponding to the first time that water reaches the production well. Accurate determination of breakthrough times is also of interest in the performance of the reservoir. Note that instead of time we plot Ψ against pore volumes injected (PVI). This is a nondimensional quantity that gives the volume of injected fluid (water in our case) as a fraction of the total pore volume. Since we are assuming constant porosity in our simulations, we have

$$\text{PVI}(t) = \int_0^t \int_0^1 \boldsymbol{n} \cdot \boldsymbol{v}(1, x_2, t) dx_2 dt. \tag{9}$$

2.2. Previous work on upscaling. The study of upscaling techniques is by no means new, and there have been many contributions to this area. Many of these are relevant to our study here, but our discussion will be limited to those closest. Most of the approaches to upscaling are designed to generate some coarse grid description which is approximately equivalent to the underlying fine grid description. Essentially, the upscaling problem for the whole system can be split into upscaling for the elliptic pressure/velocity equation (which we denote by PVE for short hereafter) and upscaling for the hyperbolic transport equation. For the PVE equation, there have been several upscaling methods developed. Since the permeability data is the principal source of the small-scale features, much effort has been devoted to methods for upscaling this quantity. Durlofsky [8] has attempted to find effective permeability properties by dividing the domain into coarse grid blocks and then solving flow problems within each of these. By averaging the resulting flow field within the coarse grid block one can obtain an effective permeability for this grid block. The full PVE is then solved in the domain with the resulting coarse grid effective permeabilities.

The multiscale finite element method (MsFEM) is a promising alternative to upscaling the permeability. In this method, coarse grid basis functions are specially constructed with subgrid features which accurately capture the fine-scale fluctuations. MsFEM has been used successfully to solve the PVE [15, 16, 14, 13, 7]. Indeed, in the upscaling scheme that we will develop we will be using a variant of this method, whereby basis functions are updated only selectively. This leads to a great saving in the amount of computation required.

The boundary conditions for the local multiscale basis functions play an essential role in upscaling of flows in porous media. On one hand, the choice of local boundary conditions for the flow within each coarse cell will affect accuracy of the resulting effective permeability. On the other hand, the performance of the upscaled equation is also sensitive to the choice of local boundary conditions (and the size of the coarse grid cell) used in the construction of the basis functions. Recent studies [6, 12] show that by using some limited global information and incorporating more accurate boundary effects into the construction of local bases, one can obtain more accurate upscaling methods, especially in the case when the permeability tensor has a strong nonlocal channelized effect. These procedures can also be used in conjunction with fine-scale velocity reconstruction techniques, which enable the fine-scale solution of the saturation equation.

Less satisfactory progress has been made in developing useful upscaling schemes for the transport equation. The methods that exist can be roughly categorized by whether they use a stochastic framework or a deterministic framework. The first approach entails a stochastic formulation of the equations, whereby the velocity and saturation fields are assumed to have a random component, corresponding to the small-scale fluctuations. The resulting flow equation for the average saturation then

incorporates the expected value and higher statistical moments of these. Langlo and Espedal [21] used this approach to upscale the saturation equation.

Efendiev, Durlofsky, and Lee [11] and Efendiev and Durlofsky [10] used a hybrid formulation, whereby the upscaled model for the saturation was developed within a fully deterministic framework, but the higher-order moments of the velocity field were modeled empirically. This was found to be successful in a range of cases, though there did exist some serious limitations. The principal difficulty with their scheme was the fact that in developing the model, fluctuations in all quantities were assumed to be small.

The approach in this work is similar to that of Efendiev, Durlofsky, and Lee [11]. The main emphasis of this work is to develop an effective scheme for upscaling the saturation equation. We will initially use a fully deterministic framework to develop an understanding of the effect of the small-scale fluctuations upon the average. This will be done at first within the restrictive assumption that all the fine-scale fluctuations are periodic. After developing the model in this way, and presenting a numerical implementation to demonstrate its validity, we will make some minor modifications that will allow us to consider the more general case where the fluctuations are nonperiodic.

3. Multiple-scale analysis. In this section we will present the framework for upscaling the porous media flow problem. We perform a multiple-scale analysis for the problem under the assumption that there exists two length scales within the problem: a large scale that captures features at the size of the domain and a small scale that captures the features within the permeability field. By doing such an analysis, with some assumptions on the nature of the small-scale features, we are able to develop equations that model the large-scale features and quantify how these are affected by the small scales. From these equations, a numerical scheme for the evolution of the average saturation can be derived easily.

We split up this section in a manner consistent with the overall solution strategy. First, we define some conventions and set up a framework in which to work. Then, we consider the multiple-scale solution for the PVE. After deriving results for the multiple-scale velocity field, we use this as a starting point for the multiple-scale analysis of the saturation equation. The results for the saturation equation, and their numerical implementation, form the main contribution of this paper. We develop a coupled set of equations for both the average and the fluctuation. The desirable features of these equations are that they capture all of the important features of the original equation and are *closed*. The closure property is often lacking in previous results, or else it is taken care of by making overly restrictive assumptions on the nature of small scales. We achieve this closure by means of a special projection, which we show is equivalent to averaging along streamlines of the flow.

3.1. Formulation of multiple-scale model. Consider first the principal source of the small scales in the porous media flow, namely the form of the permeability K. We assume that K is strongly heterogeneous and is characterized by two scales. The first is a large length scale, on the order of the size of the domain, i.e., $O(1)$, and which we denote by $\boldsymbol{x}$. The second is small length scale, of the order ϵ, with $0 < \epsilon \ll 1$. To model features at this length scale, we introduce the "fast" spatial variable $\boldsymbol{y} = \boldsymbol{x}/\epsilon$. Note that we assume that the two length scales are always distinct. This assumption may not necessarily hold for all types of permeability, but it is useful in developing our initial models. With the above length scales defined, the permeability is then

given by $K(\boldsymbol{x}, \boldsymbol{y})$. Furthermore, we may write

$$K(\boldsymbol{x}, \boldsymbol{y}) = \overline{K}(\boldsymbol{x}) + K'(\boldsymbol{x}, \boldsymbol{y}), \tag{10}$$

where $\overline{K}(\boldsymbol{x})$ represents an "average" of K and $K'(\boldsymbol{x}, \boldsymbol{y})$ is a fluctuation around this average. In general, $\overline{K}(\boldsymbol{x})$ is understood as being the weak limit of K in the limit of $\epsilon \to 0$. We assume that K is a scalar, though in general it could be a tensor.

For our analysis we make the assumption that all functions of the fast variable $\boldsymbol{y}$ are periodic with period Y and that they all lie within the space of square integrable functions. This space will be denoted in the usual way by L^2_Y. For convenience, we will always scale ϵ so that Y is the unit square $[0,1] \times [0,1]$. Note that L^2_Y is a Hilbert space if we use the scalar product

$$(u, v)_0 = (u, v)_{L^2_Y} := \int_Y u(\boldsymbol{y}) v(\boldsymbol{y}) d\boldsymbol{y} \tag{11}$$

and the corresponding norm $\| u \|_0 = \sqrt{(u, u)_0}$. Often in the sections that follow we will drop the use of the subscript 0 when writing this norm. We also introduce the related Sobolev spaces H^m_Y which consist of the set of all functions u in L^2_Y which possess weak derivatives $\partial^\alpha_y u$ in L^2_Y for all $|\alpha| \leq m$.

Since we will often using the concept of an average quantity, we make this definite by defining, for a function $\phi(\boldsymbol{x}, \boldsymbol{y})$, the average

$$\overline{\phi}(\boldsymbol{x}) = \frac{1}{|Y|} \int_Y \phi(\boldsymbol{x}, \boldsymbol{y}) d\boldsymbol{y}. \tag{12}$$

Note that this is a particular form of the expression for the weak limit of ϕ. The fluctuating part of ϕ will be denoted by ϕ' and is defined in the natural way as

$$\phi'(\boldsymbol{x}, \boldsymbol{y}) = \phi(\boldsymbol{x}, \boldsymbol{y}) - \overline{\phi}(\boldsymbol{x}). \tag{13}$$

This clearly has zero average, i.e., $\overline{\phi'} = 0$. The average (12) can be thought of as a smoothing or spatial "filtering" of the small scales (cf. Beckie, Aldama, and Wood [1]).

3.2. Upscaling for the PVE. Consider the elliptic pressure equation (4). We make the assumption (which will later be justified) that S consists of an average and a periodic fluctuating part. Then, we have $a = \lambda(S)K$, with $a = \overline{a}(\boldsymbol{x}) + a'(\boldsymbol{x}, \boldsymbol{y})$. Within the framework described above, the form of the solution can be determined using the analysis given in [2]. We look for an asymptotic expansion of the pressure in the form

$$p_\epsilon = \overline{p}(\boldsymbol{x}, \boldsymbol{y}) + \epsilon p_1(\boldsymbol{x}, \boldsymbol{y}) + \epsilon^2 p_2(\boldsymbol{x}, \boldsymbol{y}) + O(\epsilon^3), \tag{14}$$

where each of the functions p_i is periodic in $\boldsymbol{y}$. By using a multiscale expansion for p_ϵ, we can derive the homogenized equation for pressure as follows:

$$\frac{\partial}{\partial x_i} \left(a^*_{ij}(\boldsymbol{x}) \frac{\partial \overline{p}}{\partial x_j} \right) = 0, \tag{15}$$

where a^* is a diagonal tensor with

$$a^*_{ij}(\boldsymbol{x}) = \frac{1}{|Y|} \int_Y a(\boldsymbol{x}, \boldsymbol{y}) \left(1 - \frac{\partial \chi^j}{\partial y_i} \right) d\boldsymbol{y} \tag{16}$$

and χ^j is the solution of the following cell problem:

$$\frac{\partial}{\partial y_i}\left(a(\boldsymbol{x},\boldsymbol{y})\frac{\partial \chi^j}{\partial y_i}\right) = \frac{\partial a}{\partial y_j}, \tag{17}$$

with periodic boundary condition in $\boldsymbol{y}$. Moreover, the first-order corrector p_1 is given by

$$p_1(\boldsymbol{x},\boldsymbol{y}) = -\chi^j \frac{\partial \overline{p}}{\partial x_j} + \tilde{p_1}. \tag{18}$$

Thus, (15), (16), and (18) define equations for the first two terms in the expansion for the pressure (14). Note that the dependence on the fast variable $\boldsymbol{y}$ appears only at $O(\epsilon)$. We can obtain an expression for the velocity field by substituting this pressure expansion into Darcy's law. Doing this we obtain

$$\boldsymbol{v}_\epsilon = -(\overline{a}+a')\left(\frac{\partial}{\partial x_i}+\frac{1}{\epsilon}\frac{\partial}{\partial y_i}\right)(\overline{p}(\boldsymbol{x})+\epsilon p_1(\boldsymbol{x},\boldsymbol{y})+\epsilon^2 p_1(\boldsymbol{x},\boldsymbol{y})+\cdots) \tag{19}$$

$$= -(\overline{a}+a')(\nabla_x \overline{p}+\nabla_y p_1)+O(\epsilon). \tag{20}$$

Thus, $\boldsymbol{v}_\epsilon$ has the expansion

$$\boldsymbol{v}_\epsilon = \overline{\boldsymbol{v}} + \boldsymbol{v}' + \epsilon \boldsymbol{v}_1 \tag{21}$$

with

$$\overline{\boldsymbol{v}} = \overline{a}\nabla_x \overline{p} + \overline{a'\nabla_y p'}, \tag{22}$$

$$\boldsymbol{v}' = \overline{a}\nabla_y p' + a'\nabla_x \overline{p} + a'\nabla_y p' - \overline{a'\nabla_y p'}. \tag{23}$$

The expression for $\boldsymbol{v}_1$ and higher-order terms can also be derived. The analysis shows us that if we start with a permeability field with $O(1)$ fluctuations, then the resulting velocity field will also have fluctuations which are $O(1)$. As mentioned previously, since the mobility λ depends on S, the velocity field is not steady but will change as the S changes throughout the domain.

Note further that the averaged velocity field $\overline{\boldsymbol{v}}$ retains the divergence-free property, i.e., $\nabla \cdot \overline{\boldsymbol{v}} = 0$, to $O(\epsilon)$. To see this note that

$$\left(\nabla_x + \frac{1}{\epsilon}\nabla_y\right)\cdot(\overline{\boldsymbol{v}}+\boldsymbol{v}') = 0. \tag{24}$$

Equating terms with the same power of ϵ, at $O(\epsilon^{-1})$ we get $\nabla_y \cdot \boldsymbol{v}' = 0$. At $O(1)$ we have $\nabla_x \cdot (\overline{\boldsymbol{v}}+\boldsymbol{v}') = 0$. Averaging this equation over Y gives $\nabla_x \cdot \overline{\boldsymbol{v}} = 0$ and hence also $\nabla_x \cdot \boldsymbol{v}' = 0$. Therefore, we see that spatial averaging preserves the divergence-free properties.

3.3. Upscaling for the saturation equation. We now consider the problem of homogenization for the hyperbolic saturation equation

$$\frac{\partial S_\epsilon}{\partial t} + \boldsymbol{v}_\epsilon \cdot \nabla f(S_\epsilon) = 0 \tag{25}$$

in two dimensions. The incompressible velocity field $\boldsymbol{v}_\epsilon$ was shown, in the previous section, to have an $O(1)$ oscillatory component.

In the same way as for the pressure equation, we will confine our analysis to the case where the functions of the "fast" variable $\boldsymbol{y} = \boldsymbol{x}/\epsilon$ are periodic. Within this framework we will derive a closed, coupled system of equations for the average $\overline{S}$ and the $O(1)$ fluctuations S'. Closure is obtained by making use of a special *streamline* average that eliminates higher-order fluctuations. After developing these expressions we will propose some approximations that allow the methodology to be applied to more general flows for which the oscillations are not necessarily periodic with respect to the fast variable. In our case, where we are looking at flows more complex than shear flows, we will again see that the nature of the streamlines plays a very important role in determining the effective equation.

We first apply the standard multiple-scale analysis of looking for a formal expansion of the saturation of the form

$$S_\epsilon = \overline{S}(\boldsymbol{x}, t) + S'(\boldsymbol{x}, \boldsymbol{y}, t) + \epsilon S_1(\boldsymbol{x}, \boldsymbol{y}, t, \tau) + O(\epsilon^2). \tag{26}$$

Thus, S consists of an average, $\overline{S}$, modified by a fluctuating part S'. We have also introduced in this expansion a possible dependence on a fast time scale $\tau = t/\epsilon$, which appears at the $O(\epsilon)$ level. The justification for such an expansion will be probed further in section 3.3.4. As before, with the expansion for the velocity field, all the terms except $\overline{S}$ have zero mean. The flux function $f(S)$ is expanded in a similar manner:

$$f(S_\epsilon) = \overline{f}(\boldsymbol{x}, t) + f'(\boldsymbol{x}, \boldsymbol{y}, t) + \epsilon f_1(\boldsymbol{x}, \boldsymbol{y}, t, \tau) + O(\epsilon^2), \tag{27}$$

where again we have that $f', f_1, \ldots$ are periodic in $\boldsymbol{y}$ and f' has zero mean, i.e., $\overline{f'} = 0$. This expansion is determined solely from the (prescribed) form of f and S_ϵ, with

$$\overline{f} + f' = f(\overline{S} + S'), \tag{28}$$

$$f_1 = f_S S_1, \tag{29}$$

$$f_2 = f_S S_2 + \frac{1}{2} f_{SS} S_1^2, \tag{30}$$

where $f_S = \frac{df}{dS}|_{\overline{S}+S'}$, and similarly for the higher-order terms. Note that f_1, f_2, and higher-order terms do not necessarily have zero mean.

We again use that fact that for a function $\phi(\boldsymbol{x}, \boldsymbol{x}/\epsilon, t, t/\epsilon)$ we must expand the partial derivatives as

$$\nabla = \nabla_x + \frac{1}{\epsilon} \nabla_y, \tag{31}$$

$$\frac{\partial}{\partial t} = \frac{\partial}{\partial t} + \frac{1}{\epsilon} \frac{\partial}{\partial \tau}. \tag{32}$$

Substituting our expansions into the saturation equation and gathering together terms with the same power of ϵ we obtain the following hierarchy of equations:

$$\epsilon^{-1} : (\overline{\boldsymbol{v}} + \boldsymbol{v}') \cdot \nabla_y f' = 0, \tag{33}$$

$$\epsilon^0 : \frac{\partial \overline{S}}{\partial t} + \frac{\partial S'}{\partial t} + \frac{\partial S_1}{\partial \tau} + (\overline{\boldsymbol{v}} + \boldsymbol{v}') \cdot \nabla_x \overline{f} + (\overline{\boldsymbol{v}} + \boldsymbol{v}') \cdot \nabla_x f' + (\overline{\boldsymbol{v}} + \boldsymbol{v}') \cdot \nabla_y f_1 = 0, \tag{34}$$

$$\epsilon^1 : \frac{\partial S_1}{\partial t} + \frac{\partial S_2}{\partial \tau} + (\overline{\boldsymbol{v}} + \boldsymbol{v}') \cdot \nabla_x f_1 + (\overline{\boldsymbol{v}} + \boldsymbol{v}') \cdot \nabla_y f_2 = 0. \tag{35}$$

3.3.1. Framework for multiscale modeling. To facilitate the analysis, we now introduce some subspaces of L^2_Y and then several lemmas, which build a framework for multiscale analysis. The main results relate to the projection $\mathcal{P}$, given in Corollary 3.1. We first present the abstract framework and then show, in section 3.3.2, that the $\mathcal{P}$ has intuitive meaning, namely averaging along the streamlines of the flow.

We introduce the following spaces in L^2_Y:

$$\mathcal{N} = \{u \in H^1_Y : \boldsymbol{v} \cdot \nabla_y u = 0\}, \tag{36}$$

$$\mathcal{W} = \{\boldsymbol{v} \cdot \nabla_y u : u \in H^1_Y\}; \tag{37}$$

here $\boldsymbol{v}$ is our velocity field as computed from the pressure equation, so that $\nabla_y \cdot \boldsymbol{v} = 0$. We now also assume that $\boldsymbol{v}$ is bounded and that $v_i \in L^2_Y$. With these spaces, we have the following orthogonal decomposition of L^2_Y.

LEMMA 3.1.

$$L^2_Y = \mathcal{N} \oplus \overline{\mathcal{W}}. \tag{38}$$

Proof. In order to prove this lemma we need the following theorem [28].

THEOREM 3.1. *Let $\mathcal{H}$ be a Hilbert space and $\mathcal{M} \subset \mathcal{H}$ be a closed subspace. Then, any element $x \in \mathcal{H}$ has the unique decomposition $x = y + z$, with $y \in \mathcal{M}$, $z \in \mathcal{M}^\perp$, where $\mathcal{M}^\perp$ denotes the orthogonal complement of $\mathcal{M}$. Furthermore,*

$$\| x - y \| = \min_{\nu \in \mathcal{M}} \| x - \nu \|, \tag{39}$$

where $\| \cdot \|$ is the associated norm of $\mathcal{H}$.

Thus, to prove Lemma 3.1 we show that $\mathcal{N}$ and $\overline{\mathcal{W}}$ are orthogonal complements in L^2_Y. To do this, first note from their definitions that $\mathcal{N}$ and $\overline{\mathcal{W}}$ are clearly subspaces of L^2_Y (we need to take the closure of $\mathcal{W}$, since this is not a closed space). Now consider u such that $(u, \boldsymbol{v} \cdot \nabla_y w) = 0$ is satisfied for each $w \in H^1_Y$. This implies that $(\boldsymbol{v} \cdot \nabla_y u, w) = 0$ for each $w \in H^1_Y$ and hence $u \in \mathcal{N}$. Since $\boldsymbol{v} \cdot \nabla_y w \in \overline{\mathcal{W}}$ we therefore have $\overline{\mathcal{W}} \perp \mathcal{N}$ in L^2_Y. Because L^2_Y is a Hilbert space all the hypotheses of Theorem 3.1 are satisfied, and thus Lemma 3.1 follows.

In Theorem 3.1, the element $y \in \mathcal{M}$ is called the *orthogonal projection* of x onto $\mathcal{M}$ and the abstract form of the projection is given by (39). To derive a more explicit form for the projection in our case, consider using $\mathcal{M} = \mathcal{W}$ in the theorem. Then, from the definition (37) for $\mathcal{W}$, for a given $u \in L^2_Y$ the projection $\mathcal{Q} : L^2_Y \mapsto \mathcal{W}$ is then defined as the solution of the minimization problem

$$\| u - \mathcal{Q}(u) \| = \min_{\theta \in H^1_Y} \| u - \boldsymbol{v} \cdot \nabla_y \theta \|, \tag{40}$$

where $\| \cdot \|$ is the L^2_Y-norm. If we had an orthonormal basis for $\mathcal{W}$ (or its restriction to a finite dimensional subspace), then we could use a least-squares approximation to determine the solution to this problem. In the absence of possessing such a basis we use the following lemma.

LEMMA 3.2. *For $u \in H^1_Y$ the projection $\mathcal{Q} : H^1_Y \mapsto \mathcal{W}$ is uniquely given by $\mathcal{Q}(u) = \boldsymbol{v} \cdot \nabla_y \theta$, where $\theta \in H^1_Y$ is the solution of the degenerate elliptic PDE*

$$\nabla_y \cdot (A \nabla_y \theta) = \boldsymbol{v} \cdot \nabla_y u \tag{41}$$

with periodic boundary conditions, where A is the 2×2 matrix with components $A_{ij} = v_i v_j$.

Proof. First, expand the norm in (40) via

$$\begin{aligned}\| u - \boldsymbol{v} \cdot \nabla_y \theta \|^2 &= \int_Y (u - \boldsymbol{v} \cdot \nabla_y \theta)^2 \, d\boldsymbol{y} \\ &= \int_Y \left(u^2 + 2\theta v_i \frac{\partial u}{\partial y_i} + v_i v_j \frac{\partial \theta}{\partial y_i} \frac{\partial \theta}{\partial y_j} \right) d\boldsymbol{y},\end{aligned}$$

where we have used integration by parts and $\nabla_y \cdot \boldsymbol{v} = 0$. Defining

$$a(\psi, \phi) = \int_Y v_i v_j \frac{\partial \psi}{\partial y_i} \frac{\partial \phi}{\partial y_i} d\boldsymbol{y} \, , \qquad h(u, \phi) = \int_Y \phi v_i \frac{\partial u}{\partial y_j} d\boldsymbol{y}, \tag{42}$$

then the minimization problem (40) is equivalent to finding the minimum of

$$J(\theta) := \frac{1}{2} a(\theta, \theta) + h(u, \theta) \tag{43}$$

over H^1_Y. It is easy to see that $a(\psi, \phi)$ is a symmetric *semipositive* bilinear form, i.e., $a(\psi, \psi) \geq 0$ for all $\psi \in H^1_Y$. $a(\psi, \psi)$ is not positive, since we can see from its definition that it is zero for $\psi \in \mathcal{N} \cap H^1_Y$. However, for $\phi \in H^1_Y - \mathcal{N}$, $\phi \neq 0$ we have $a(\phi, \phi) > 0$. It is easy to show that $J(\theta)$ attains its minimum over H^1_Y at θ if and only if

$$a(\theta, \phi) = h(u, \phi) \tag{44}$$

for all $\phi \in H^1_Y$ and that this minimum is unique up to a function in $\mathcal{N}$.

Note that A has eigenvalues $\lambda = 0, v_1^2 + v_2^2$, and therefore (41) is a degenerate elliptic equation.

Integration by parts of (44) and using the fact that $\nabla_y \cdot \boldsymbol{v} = 0$ gives

$$\int_Y \phi \frac{\partial}{\partial y_i} \left(v_i v_j \frac{\partial \theta}{\partial y_j} \right) d\boldsymbol{y} = \int_Y \phi v_i \frac{\partial u}{\partial y_i} d\boldsymbol{y} \tag{45}$$

for all $\phi \in H^1_Y$, from which (41) follows. Returning to (40) we see that $\boldsymbol{v} \cdot \nabla_y \theta$ is the unique minimizer over H^1_Y, which proves the lemma.

With the projection $\mathcal{Q}$ defined, we immediately have from Lemmas 3.1 and 3.2 the following corollary.

COROLLARY 3.1. *For $u \in H^1_Y$ the projection $\mathcal{P} : H^1_Y \mapsto \mathcal{N}$ is uniquely given by $\mathcal{P}(u) = u - \mathcal{Q}(u)$.*

It is clear that $\mathcal{P}$ and $\mathcal{Q}$ are linear. We remark that the projection $\mathcal{P}$ from H^1_Y to $\mathcal{N}$ has also been used in [9]. In order to make full use of the projections, we now present several simple but useful lemmas.

LEMMA 3.3. *For $w \in \mathcal{W}$ we have $\mathcal{Q}(w) = w$.*

Proof. Since $w \in \mathcal{W}$, then $w = \boldsymbol{v} \cdot \nabla_y u$ for some $u \in H^1_Y$. Then, from Lemma 3.2 we have $\mathcal{Q}(w) = \boldsymbol{v} \cdot \nabla_y \theta$, where θ is the periodic solution of

$$\begin{aligned}\nabla_y \cdot (A \nabla_y \theta) &= \boldsymbol{v} \cdot \nabla_y w \\ &= \boldsymbol{v} \cdot \nabla_y (\boldsymbol{v} \cdot \nabla_y u) \\ &= \nabla_y \cdot (A \nabla_y u) \, .\end{aligned}$$

Thus, using the analysis in Lemma 3.2, $\theta = u$ uniquely up to function in $\mathcal{N}$. Then,

$$\mathcal{Q}(w) = \boldsymbol{v} \cdot \nabla_y \theta = \boldsymbol{v} \cdot \nabla_y u = w. \tag{46}$$

LEMMA 3.4. *For $u \in \mathcal{N}$ we have $\mathcal{Q}(u) = 0$.*

Proof. Consider $v = u + w$, where $w \in \mathcal{W}$. Then, taking the $\mathcal{Q}$ projection gives

$$\mathcal{Q}(v) = \mathcal{Q}(u) + \mathcal{Q}(w) = \mathcal{Q}(u) + w \tag{47}$$

using Lemma 3.3. Then, subtracting this from $v = u + w$ and rearranging gives

$$v - \mathcal{Q}(v) - u = -\mathcal{Q}(u). \tag{48}$$

Since $v - \mathcal{Q}(v) \in \mathcal{N}$ and $u \in \mathcal{N}$ the left-hand side is in $\mathcal{N}$. But $\mathcal{Q}(u) \in \mathcal{W}$, and since $\mathcal{N} \cap \mathcal{W} = \{0\}$ we must therefore have $\mathcal{Q}(u) = 0$.

COROLLARY 3.2. *For $u \in \mathcal{N}$ we have $\mathcal{P}(u) = u$.*

COROLLARY 3.3. *For $w \in \mathcal{W}$ we have $\mathcal{P}(w) = 0$.*

LEMMA 3.5. *For each $u \in H^1_Y$ we have*

$$\overline{\mathcal{P}(u)} = \overline{u}. \tag{49}$$

Proof. Using the expression for $\mathcal{P}(u) = u - \mathcal{Q}(u)$ we have

$$\overline{\mathcal{P}(u)} = \overline{u - \mathcal{Q}(u)} = \overline{u} - \overline{\mathcal{Q}(u)}.$$

Using the expression for the projection $\mathcal{Q}(u)$ and the definition for the average gives

$$\overline{\mathcal{Q}(u)} = \int_Y \mathcal{Q}(u) d\boldsymbol{y} = \int_Y \boldsymbol{v} \cdot \nabla_y \theta d\boldsymbol{y} = 0,$$

since $\nabla_y \cdot \boldsymbol{v} = 0$ and thus (49).

LEMMA 3.6. *If $u, w \in \mathcal{N}$, then $uw \in \mathcal{N}$.*

Proof. This is simply proved by expanding

$$\boldsymbol{v} \cdot \nabla_y (uw) = w(\boldsymbol{v} \cdot \nabla_y u) + u(\boldsymbol{v} \cdot \nabla_y w) = 0. \tag{50}$$

LEMMA 3.7. *For each $u \in H^1_Y$, $v \in \mathcal{N}$ we have*

$$(\mathcal{P}(u), v) = (u, v). \tag{51}$$

Proof. From Lemma 3.1 and Lemma 3.4 we have $u = \mathcal{P}(u) + w$ with $w \in \overline{\mathcal{W}}$. Then

$$(u, v) = (\mathcal{P}(u) + w, v) = (\mathcal{P}(u), v) + (w, v) = (\mathcal{P}(u), v), \tag{52}$$

since $\mathcal{W} \perp \mathcal{N}$.

LEMMA 3.8. *If $w \in \mathcal{N}$, then $\mathcal{P}(wv) = w\mathcal{P}(v)$ for each $v \in H^1_Y$.*

Proof. For any $u \in H^1_Y$ we have

$$(\mathcal{P}(wv), u) = (\mathcal{P}(wv), \mathcal{P}(u)) = (wv, \mathcal{P}(u)) = (v, w\mathcal{P}(u)). \tag{53}$$

Since $w\mathcal{P}(u)$ is also in $\mathcal{N}$ by Lemma 3.6, we have

$$(v, w\mathcal{P}(u)) = (\mathcal{P}(v), w\mathcal{P}(u)) = (w\mathcal{P}(v), \mathcal{P}(u)) = (w\mathcal{P}(v), u), \tag{54}$$

where we have used again Lemma 3.6 to show that $w\mathcal{P}(v)$ is in $\mathcal{N}$. Thus, $(\mathcal{P}(wv), u) = (w\mathcal{P}(v), u)$ for any $u \in H^1_Y$, and the lemma follows.

LEMMA 3.9. *$\mathcal{P}(u)$ and $\mathcal{Q}(u)$ are unchanged if we multiply the velocity field $\boldsymbol{v}$ by $\psi \in \mathcal{N}$, $\psi \neq 0$.*

Proof. We have $\mathcal{Q}(u) = \boldsymbol{v} \cdot \nabla_y \theta$, where θ is the periodic solution of (41). Then, consider the projection with velocity field $\mathbf{u} = \psi \boldsymbol{v}$, i.e., $\mathcal{Q}^*(u) = \psi \boldsymbol{v} \cdot \nabla_y \theta^*$, where θ^* satisfies

$$\psi \boldsymbol{v} \cdot \nabla_y \left(\psi \boldsymbol{v} \cdot \nabla_y \theta^* \right) = \psi \boldsymbol{v} \cdot \nabla_y u. \tag{55}$$

Since $\psi \in \mathcal{N}$, $\psi \neq 0$ this gives

$$\boldsymbol{v} \cdot \nabla_y \left(\boldsymbol{v} \cdot \nabla_y (\psi \theta^*) \right) = \boldsymbol{v} \cdot \nabla_y u. \tag{56}$$

Therefore, $\psi \theta^* = \theta$ up to a function in $\mathcal{N}$. But then $\psi \boldsymbol{v} \cdot \nabla_y \theta^* = \boldsymbol{v} \cdot \nabla_y (\psi \theta^*) = \boldsymbol{v} \cdot \nabla_y \theta$ so that $\mathcal{Q}^*(u) = \mathcal{Q}(u)$. Since $\mathcal{P}(u) = u - \mathcal{Q}(u)$ this is also unchanged.

LEMMA 3.10. *For $v, w \in H^1_Y$ we have*

$$(\mathcal{Q}(v), \boldsymbol{v} \cdot \nabla_y w) = (v, \boldsymbol{v} \cdot \nabla_y w). \tag{57}$$

Proof. By simple substitution we have

$$\begin{aligned} (\mathcal{Q}(v), \boldsymbol{v} \cdot \nabla_y w) &= (v - \mathcal{P}(v), \boldsymbol{v} \cdot \nabla_y w) \\ &= (v, \boldsymbol{v} \cdot \nabla_y w) - (\mathcal{P}(v), \boldsymbol{v} \cdot \nabla_y w) \\ &= (v, \boldsymbol{v} \cdot \nabla_y w), \end{aligned} \tag{58}$$

since $\mathcal{P}(v) \in \mathcal{N}$, $\boldsymbol{v} \cdot \nabla_y w \in \mathcal{W}$, and $\mathcal{W} \perp \mathcal{N}$.

LEMMA 3.11. *If $u \in \mathcal{N}$, then*

$$(\mathcal{Q}(\partial_{x_i} u), \boldsymbol{v} \cdot \nabla_y w) = -(u, (\partial_{x_i} \boldsymbol{v}) \cdot \nabla_y w) \tag{59}$$

and

$$(\mathcal{Q}(\partial_t u), \boldsymbol{v} \cdot \nabla_y w) = -(u, (\partial_t \boldsymbol{v}) \cdot \nabla_y w) \tag{60}$$

hold for all $w \in H^1_Y$.

Proof. In Lemma 3.10 let $v = \frac{\partial u}{\partial x_1}$, where $u \in \mathcal{N}$. By definition, we have $\boldsymbol{v} \cdot \nabla_y u = 0$, and

$$\frac{\partial}{\partial x_1} (\boldsymbol{v} \cdot \nabla_y u) = \frac{\partial v_i}{\partial x_1} \frac{\partial u}{\partial y_i} + v_i \frac{\partial^2 u}{\partial x_1 \partial y_i} = 0. \tag{61}$$

Thus, we have

$$\frac{\partial v_i}{\partial x_1} \frac{\partial u}{\partial y_i} = -v_i \frac{\partial^2 u}{\partial x_1 \partial y_i}. \tag{62}$$

Now using (62) and Lemma 3.10 with $\mathcal{Q}(\partial_{x_1} u)$ we get

$$\begin{aligned} \left(\mathcal{Q}\left(\frac{\partial u}{\partial x_1} \right), \boldsymbol{v} \cdot \nabla_y w \right) &= \left(\frac{\partial u}{\partial x_1}, \boldsymbol{v} \cdot \nabla_y w \right) \\ &= \left(\frac{\partial u}{\partial x_1}, \nabla_y \cdot (\boldsymbol{v} w) \right) \\ &= -\int_Y v_i w \frac{\partial^2 u}{\partial x_1 \partial y_i} d\boldsymbol{y} \\ &= \int_Y w \frac{\partial v_i}{\partial x_1} \frac{\partial u}{\partial y_i} d\boldsymbol{y}. \end{aligned}$$

Integration by parts on this gives us

$$-\int_Y u\frac{\partial}{\partial y_i}\left(w\frac{\partial v_i}{\partial x_1}\right)d\boldsymbol{y} = -\int_Y u\left[\frac{\partial v_i}{\partial x_1}\frac{\partial w}{\partial y_i} + w\frac{\partial}{\partial x_1}\left(\frac{\partial v_i}{\partial y_i}\right)\right]d\boldsymbol{y} \tag{63}$$

$$= -\int_Y u\left(\frac{\partial v_i}{\partial x_1}\frac{\partial w}{\partial y_i}\right)d\boldsymbol{y} \tag{64}$$

using the fact that $\nabla_y \cdot \boldsymbol{v} = 0$. Thus we obtain the lemma. The other results are derived in an exactly similar manner.

Lemma 3.11 is very useful, since it provides an alternative means of calculating the quantity $\mathcal{Q}(\partial_t u)$, which can be seen from the following lemma.

LEMMA 3.12. *For $u \in H^1_Y$ the projection $\mathcal{Q}(\partial_t u)$ can be uniquely determined by $\mathcal{Q}(\partial_t u) = \boldsymbol{v} \cdot \nabla_y \phi$, where ϕ is the solution of the degenerate elliptic PDE*

$$\nabla_y \cdot (A\nabla_y \phi) = -\frac{\partial \boldsymbol{v}}{\partial t} \cdot \nabla_y u \tag{65}$$

with periodic boundary conditions, where A is the 2×2 matrix with components $A_{ij} = v_i v_j$.

Proof. From the proof of Lemma 3.2 we know that (65) has a solution which is unique up to a function in $\mathcal{N}$. For all $w \in H^1_Y$ we have, using the definition for ϕ, that

$$\begin{aligned}
(\boldsymbol{v}\cdot\nabla_y\phi, \boldsymbol{v}\cdot\nabla_y w) &= \int_Y v_i v_j \frac{\partial \phi}{\partial y_i}\frac{\partial w}{\partial y_j} d\boldsymbol{y} \\
&= -\int_Y w\frac{\partial}{\partial y_i}\left(v_i v_j \frac{\partial \phi}{\partial y_j}\right)d\boldsymbol{y} \\
&= \int_Y w\frac{\partial v_i}{\partial t}\frac{\partial u}{\partial y_i} d\boldsymbol{y} \\
&= \int_Y w\frac{\partial}{\partial y_i}\left(u\frac{\partial v_i}{\partial t}\right)d\boldsymbol{y} \\
&= -\int_Y u\frac{\partial v_i}{\partial t}\frac{\partial w}{\partial y_j} d\boldsymbol{y} \\
&= -\left(u, (\partial_t \boldsymbol{v})\cdot\nabla_y w\right).
\end{aligned}$$

From Lemma 3.11 we also have that

$$(\mathcal{Q}(\partial_t u), \boldsymbol{v}\cdot\nabla_y w) = -\left(u, (\partial_t \boldsymbol{v})\cdot\nabla_y w\right) \tag{66}$$

holds for all $w \in H^1_Y$. Since $\boldsymbol{v}\cdot\nabla_y w$ spans $\overline{\mathcal{W}}$, we therefore have that $\mathcal{Q}(\partial_t u) = \boldsymbol{v}\cdot\nabla_y\phi$ uniquely determines the projection.

An exactly similar result holds for the projection $\mathcal{Q}(\partial_{x_i} u)$. From the above lemma, we see that $\mathcal{Q}(\partial_t u)$ can be found without explicitly calculating $\partial_t u$. This will be useful in the development of a numerical scheme later on.

3.3.2. An alternative derivation for the projection. Another, more intuitively meaningful form of the projection $\mathcal{P}$ can be derived. From Lemma 3.1 and (41) we have $\mathcal{P}(u) = u - \boldsymbol{v}\cdot\nabla_y\theta$, where θ is the solution of (41). In this equation the matrix A is symmetric, and therefore we can write it in the diagonal form $A = TDT^T$, where T is an orthonormal matrix

$$T = \frac{1}{\sqrt{v_1^2+v_2^2}}\begin{pmatrix} v_1 & v_2 \\ v_2 & -v_1 \end{pmatrix}, \qquad D = \begin{pmatrix} v_1^2+v_2^2 & 0 \\ 0 & 0 \end{pmatrix}. \tag{67}$$

Note that A is singular and hence D has only a single no-zero diagonal element. Now introduce a new set of coordinates $\tilde{y}$ such that $\nabla_{\tilde{y}} = T\nabla_y$. Then, (41) can be written using the $\tilde{y}$ variables as

$$\nabla_{\tilde{y}} \cdot \left(D\nabla_{\tilde{y}}\tilde{\theta} \right) = \boldsymbol{v} \cdot \left(T^{-1}\nabla_{\tilde{y}}\tilde{u} \right), \tag{68}$$

where $\tilde{\theta}(\tilde{y}_1, \tilde{y}_2) = \theta(y_1, y_2)$, and similarly for $\tilde{u}$. Expanding and simplifying the right-hand side and also using the form of the matrix D we obtain the much simpler equation

$$\frac{\partial}{\partial \tilde{y}_1}\left[(v_1^2 + v_2^2)\frac{\partial \tilde{\theta}}{\partial \tilde{y}_1} \right] = \sqrt{v_1^2 + v_2^2}\frac{\partial \tilde{u}}{\partial \tilde{y}_1}, \tag{69}$$

which contains only the $\tilde{y}_1$-derivatives. Solving for $\tilde{\theta}$ from this gives

$$\tilde{\theta} = \int_0^{\tilde{y}_1} \frac{1}{v_1^2 + v_2^2} \int_0^{\eta} \sqrt{v_1^2 + v_2^2}\frac{\partial \tilde{u}}{\partial \tilde{y}_1} d\xi d\eta + c\int_0^{\tilde{y}_1} \frac{1}{v_1^2 + v_2^2} d\eta + d, \tag{70}$$

where $c = c(\tilde{y}_2, t)$ and $d = d(\tilde{y}_2, t)$ are to be determined, and η is the dummy variable for $\tilde{y}_1$ in the integration. From Lemma 3.2, the projection is computed as $\mathcal{Q}(u) = \boldsymbol{v} \cdot \nabla_y \theta$, and in the new coordinates $(\tilde{y}_1, \tilde{y}_2)$, using (70) this gives

$$\mathcal{Q}(u) = \sqrt{v_1^2 + v_2^2}\frac{\partial \tilde{\theta}}{\partial \tilde{y}_1} = \frac{1}{\sqrt{v_1^2 + v_2^2}} \int_0^{\tilde{y}_1} \sqrt{v_1^2 + v_2^2}\frac{\partial \tilde{u}}{\partial \tilde{y}_1} d\eta + \frac{c}{\sqrt{v_1^2 + v_2^2}}. \tag{71}$$

The constants in (70) are determined from the boundary conditions.

Now consider a particular fluid particle on the streamlines $\boldsymbol{z}(\tau)$, i.e., a *Lagrangian* description, with coordinates $(\tilde{y}_1, \tilde{y}_2)$. In view of the fact that $\tilde{y}_1$ is the arc length along a streamline this means that we must have

$$\frac{d\tilde{y}_1}{d\tau} = \sqrt{v_1^2 + v_2^2}. \tag{72}$$

If we further assume that $\sqrt{v_1^2 + v_2^2}$ is slowly varying in τ, which is reasonable, since the velocity field and streamlines are slowly varying with time, after some algebra, we can derive the following equivalent definition of the projection $\mathcal{P}$ (see [27] for more detailed derivations).

LEMMA 3.13. *The projection $\mathcal{P} : H^1_Y \mapsto \mathcal{N}$ is uniquely given by*

$$\mathcal{P}(u)(\boldsymbol{x}, \boldsymbol{y}, t) = \lim_{T\to\infty} \frac{1}{T}\int_0^T u(\boldsymbol{x}, \boldsymbol{\Theta}(s), t, s) ds, \tag{73}$$

where $\boldsymbol{\Theta}(\boldsymbol{x}, t, \tau; \boldsymbol{y})$ is the flow map defined by

$$\frac{d\boldsymbol{\Theta}}{d\tau} = \boldsymbol{v}, \qquad \boldsymbol{\Theta}(0) = \boldsymbol{y}. \tag{74}$$

The interpretation of the projection $\mathcal{P}(u)$ is now obvious. It is the average of the quantity u along the streamlines, and we therefore will refer to it as the *streamline* averaging. It is the natural complement to the spatial average for this problem: the spatial average eliminates dependence on the fast spatial scales; the streamline average eliminates dependence on the fast time scales.

3.3.3. Derivation of the upscaling equation for saturation. We are now ready to derive the upscaling equation for the transport equation for saturation. Consider again our set of equations from the multiscale expansion. From the $O(\epsilon^{-1})$ equation

$$\boldsymbol{v} \cdot \nabla_y f' = 0 \tag{75}$$

we have $f' \in \mathcal{N}$. Recalling that f' is determined from $f' = f(\overline{S} + S') - \overline{f}$ and that $f(S)$ is smooth and $\overline{f}$ is independent of $\boldsymbol{y}$ we have

$$\boldsymbol{v} \cdot \nabla_y \left[f(\overline{S} + S') - \overline{f} \right] = f_S \boldsymbol{v} \cdot \nabla_y S', \tag{76}$$

where

$$f_S = \left. \frac{df}{dS} \right|_{\overline{S}+S'}. \tag{77}$$

Thus, from this we see that we have $S' \in \mathcal{N}$, provided that $f_S \neq 0$. From (6), $f(S)$ is given by $f(S) = \frac{S^2}{S^2 + a(1-S)^2}$ with $a > 0$ so that

$$\frac{df}{dS} = \frac{2aS(1-S)}{(S^2 + a(1-S)^2)^2}. \tag{78}$$

From this we see that (77) is zero for $\overline{S} + S' = 0, 1$ only. However, note that if $\overline{S} = 1$, then this implies that $S' \equiv 0$ in the cell and therefore $\boldsymbol{v} \cdot \nabla_y S' = 0$, and similarly for the case of $\overline{S} = 0$. If $\overline{S} \neq 0, 1$ and $\overline{S} + S' = 1$, then we must clearly have $\frac{\partial S'}{\partial y_1} = 0$ and $\frac{\partial S'}{\partial y_2} = 0$ (since it is a maximum) and hence $\boldsymbol{v} \cdot \nabla_y S' = 0$. The same argument holds for the case where $\overline{S} + S' = 0$ and where S' must be a minimum. Thus, we can conclude that $S' \in \mathcal{N}$ everywhere.

Equation (76) provides only a constraint that $S' \in \mathcal{N}$, but S' cannot be solved for directly from this equation. In order to determine S' we will need to develop a second equation that describes its evolution in time.

Now consider the $O(\epsilon^0)$ equation. Taking the spatial average of this equation and using that fact that all fluctuating terms have zero mean gives us, upon rearrangement,

$$\frac{\partial \overline{S}}{\partial t} + \overline{\boldsymbol{v}} \cdot \nabla_x \overline{f} = -\nabla_x \cdot \overline{\boldsymbol{v}' f'}. \tag{79}$$

This equation is basically similar to our original equation (25), since we have $\nabla_x \cdot \overline{\boldsymbol{v}} = 0$, and so the homogeneous part gives a conservation law for $\overline{S}$. The right-hand side term corresponds to the interaction of the small-scale fluctuations upon the large-scale average. The overall nature of this equation is not immediately clear without knowledge of the flux fluctuation f'. The essence of the upscaling problem is how to accurately compute this term without computing the actual fluctuations S' at all points. Towards this end, we first derive the equation for S'. Subtract (79) from (34) to obtain

$$\frac{\partial S'}{\partial t} + \boldsymbol{v}' \cdot \nabla_x \overline{f} + (\overline{\boldsymbol{v}} + \boldsymbol{v}') \cdot \nabla_x f' + \frac{\partial S_1}{\partial \tau} + (\overline{\boldsymbol{v}} + \boldsymbol{v}') \cdot \nabla_y f_1 - \nabla_x \cdot \overline{\boldsymbol{v}' f'} = 0. \tag{80}$$

We now apply the $\mathcal{P}$ projection to this equation. Consider each of the terms: for the first term we have

$$\mathcal{P}\left(\frac{\partial S'}{\partial t} \right) = \frac{\partial S'}{\partial t} - \mathcal{Q}\left(\frac{\partial S'}{\partial t} \right). \tag{81}$$

The second term on the right-hand side is computable without having to evaluate $\frac{\partial S'}{\partial t}$ if we use Lemma 3.12, since $S' \in \mathcal{N}$ (only knowledge of S' and $\frac{\partial S'}{\partial t}$ is needed). This is useful, since we obtain the time derivative in explicit form. Next, using $\frac{\partial \overline{f}}{\partial x_i} \in \mathcal{N}$ (since it has no y-dependence) and Lemma 3.8 we have

$$\mathcal{P}\left(\boldsymbol{v}' \cdot \nabla_x \overline{f}\right) = \mathcal{P}\left(\boldsymbol{v}'\right) \cdot \nabla_x \overline{f}, \tag{82}$$

where $\mathcal{P}\left(\boldsymbol{v}'\right) = (\mathcal{P}(v_1), \mathcal{P}(v_2))$. Similarly, we have

$$\mathcal{P}\left(\nabla_x \cdot \overline{\boldsymbol{v}' f'}\right) = \nabla_x \cdot \overline{\boldsymbol{v}' f'}, \tag{83}$$

since there is no y-dependence. The projection of the other terms in the equation are more complicated to evaluate. First, consider the third term of (80)

$$\mathcal{P}\left((\overline{\boldsymbol{v}} + \boldsymbol{v}') \cdot \nabla_x f'\right) = \mathcal{P}\left(\overline{\boldsymbol{v}} \cdot \nabla_x f'\right) + \mathcal{P}\left(\boldsymbol{v}' \cdot \nabla_x f'\right). \tag{84}$$

For the first of the term in (84),

$$\mathcal{P}\left(\overline{\boldsymbol{v}} \cdot \nabla_x f'\right) = \overline{\boldsymbol{v}} \cdot \mathcal{P}\left(\nabla_x f'\right) \tag{85}$$

$$= \overline{\boldsymbol{v}} \cdot \nabla_x f' - \overline{\boldsymbol{v}} \cdot \mathcal{Q}\left(\nabla_x f'\right). \tag{86}$$

For the second term in (84) we have

$$\mathcal{P}\left(\boldsymbol{v}' \cdot \nabla_x f'\right) = \mathcal{P}\left((\mathcal{P}(\boldsymbol{v}') + \mathcal{Q}(\boldsymbol{v}')) \cdot \nabla_x f'\right) \tag{87}$$

$$= \mathcal{P}\left(\mathcal{P}(\boldsymbol{v}') \cdot \nabla_x f'\right) + \mathcal{P}\left(\mathcal{Q}(\boldsymbol{v}') \cdot \nabla_x f'\right). \tag{88}$$

For the first term in (88) we use Lemma 3.8 to obtain

$$\begin{aligned}\mathcal{P}\left(\mathcal{P}(\boldsymbol{v}') \cdot \nabla_x f'\right) &= \mathcal{P}(\boldsymbol{v}') \cdot \mathcal{P}\left(\nabla_x f'\right) \\ &= \mathcal{P}(\boldsymbol{v}') \cdot \nabla_x f' - \mathcal{P}(\boldsymbol{v}') \cdot \mathcal{Q}\left(\nabla_x f'\right)\end{aligned}$$

and for the second term in (88) we have

$$\begin{aligned}\mathcal{P}\left(\mathcal{Q}(\boldsymbol{v}') \cdot \nabla_x f'\right) &= \mathcal{P}\left(\mathcal{Q}(\boldsymbol{v}') \cdot \left(\mathcal{P}\left(\nabla_x f'\right) + \mathcal{Q}\left(\nabla_x f'\right)\right)\right) \\ &= \mathcal{P}\left(\mathcal{Q}(\boldsymbol{v}') \cdot \mathcal{P}\left(\nabla_x f'\right)\right) + \mathcal{P}\left(\mathcal{Q}(\boldsymbol{v}') \cdot \mathcal{Q}\left(\nabla_x f'\right)\right) \\ &= \mathcal{P}\left(\mathcal{Q}(\boldsymbol{v}') \cdot \mathcal{Q}\left(\nabla_x f'\right)\right).\end{aligned}$$

Thus, we obtain

$$\mathcal{P}\left((\overline{\boldsymbol{v}} + \boldsymbol{v}') \cdot \nabla_x f'\right) = (\overline{\boldsymbol{v}} + \mathcal{P}(\boldsymbol{v}')) \cdot \nabla_x f' - (\overline{\boldsymbol{v}} + \mathcal{P}(\boldsymbol{v}')) \cdot \mathcal{Q}\left(\nabla_x f'\right) + \mathcal{P}\left(\mathcal{Q}(\boldsymbol{v}') \cdot \mathcal{Q}\left(\nabla_x f'\right)\right). \tag{89}$$

Now consider the projection of the remaining terms which involve the fast time τ:

$$\mathcal{P}\left(\frac{\partial S_1}{\partial \tau} + (\overline{\boldsymbol{v}} + \boldsymbol{v}') \cdot \nabla_y f_1\right). \tag{90}$$

From (29) we have $f_1 = f_S S_1$. Note that $\boldsymbol{v} \cdot \nabla_y f_S = 0$, since $f_S = \frac{df}{dS}|_{\overline{S}+S'}$, and therefore $\boldsymbol{v} \cdot \nabla_y S' = 0$ ($f_{SS} = 0$ only at values of S less than the shock height). Thus,

$$\frac{\partial S_1}{\partial \tau} + (\overline{\boldsymbol{v}} + \boldsymbol{v}') \cdot \nabla_y f_1 = \frac{\partial S_1}{\partial \tau} + f_S(\overline{\boldsymbol{v}} + \boldsymbol{v}') \cdot \nabla_y S_1. \tag{91}$$

If we project the right-hand side of this equation onto streamlines $\tilde{\boldsymbol{z}}$ defined the velocity field $f_S \boldsymbol{v}$, then this becomes the total derivative $\frac{dS_1}{d\tilde{\boldsymbol{z}}}$. By Lemma 3.9, the projection $\mathcal{P}$ is unchanged by multiplying the velocity field by a function $g \in \mathcal{N}$. Therefore, using the alternative form of the projection, with $f_S \boldsymbol{v}$ instead of $\boldsymbol{v}$ we get

$$\begin{aligned}\mathcal{P}\left(\frac{\partial S_1}{\partial \tau} + f_S(\overline{\boldsymbol{v}} + \boldsymbol{v}') \cdot \nabla_y S_1\right) &= \lim_{T\to\infty} \frac{1}{T}\int_0^T \frac{dS_1}{d\tilde{\boldsymbol{z}}} d\tau \\ &= \lim_{T\to\infty} \frac{S_1(T) - S_1(0)}{T} \\ &= 0\end{aligned}$$

if S_1 is bounded.

Combining the above results, we obtain the following theorem.

THEOREM 3.2. *For the ansatz* (26)*, $\overline{S}$ and S' satisfy the following closed, coupled system of equations:*

$$\frac{\partial \overline{S}}{\partial t} + \overline{\boldsymbol{v}} \cdot \nabla_x \overline{f} + \nabla_x \cdot \overline{\boldsymbol{v}' f'} = 0, \tag{92}$$

$$\frac{\partial S'}{\partial t} + (\overline{\boldsymbol{v}} + \mathcal{P}(\boldsymbol{v}')) \cdot \nabla_x f' + \mathcal{P}\left(\boldsymbol{v}'\right) \cdot \nabla_x \overline{f} - \nabla_x \cdot \overline{\boldsymbol{v}' f'} = G(\boldsymbol{x}, \boldsymbol{y}, t), \tag{93}$$

where

$$G(\boldsymbol{x}, \boldsymbol{y}, t) = (\overline{\boldsymbol{v}} + \mathcal{P}(\boldsymbol{v}')) \cdot \mathcal{Q}\left(\nabla_x f'\right) - \mathcal{P}\left(\mathcal{Q}(\boldsymbol{v}') \cdot \mathcal{Q}\left(\nabla_x f'\right)\right) + \mathcal{Q}\left(\frac{\partial S'}{\partial t}\right). \tag{94}$$

Furthermore, for each fixed $\boldsymbol{y}$ the system is hyperbolic with respect to variables $\boldsymbol{x}$ and t.

Proof. Combining the previous results gives us the form of the equations. We therefore need only demonstrate that the system is hyperbolic in the variables $\boldsymbol{x}$ and t (note that the fast spatial variable $\boldsymbol{y}$ now appears only as a parameter in the above system and also that the fast time τ has been completely eliminated). Hyperbolicity has been proved in [27].

Note that the our system (92) and (93) is not in conservation form, even though the original equation (25) defines a conservation law. This is due to the fact that the original saturation has been split as $S_\epsilon = \overline{S} + S' + O(\epsilon)$.

In deriving our set of equations (92) and (93) we employ streamline averaging to eliminate, from the fluctuation equation, "memory effects" [26] at the small scale, which are persistent due to the absence of dispersion. In fact, the memory effect is already incorporated implicitly by the streamline projection together with the use of the cell problem, which characterize the fluctuation at small scales. One can see this by formally substituting the fluctuation equation into the average equation and retaining only the leading-order term if we assume that the fluctuation is small. The novelty of the multiscale analysis presented here is that we can derive a closed system for the homogenized equation without assuming that the fluctuation is small. Further, the resulting homogenized equation is amenable to computation. Previous works on purely hyperbolic transport, e.g., [17] or [26], have not been able to derive a computationally effective homogenization equation for the transport equation. Either an infinite coupled hyperbolic system is derived in the case of [17] or a Young measure is introduced in the case of [26]. In both cases, the homogenization equation cannot be used directly for practical computations.

3.3.4. Justification for the asymptotic expansions. In our analysis we have been deliberately vague with the choice of initial conditions for the terms in the expansion of the saturation. This is due to the fact that terms involving the fast time scale τ appear in the analytic solution but do not generally appear if we start from smooth initial data (i.e., the initial saturation is a function of the large scale $\boldsymbol{x}$ only). To see this, we write the solution of (25) as $S_\epsilon = \hat{S}(\boldsymbol{x}, \boldsymbol{y}, t) + \tilde{S}(\boldsymbol{x}, \boldsymbol{y}, t, \tau)$, i.e., an "average" with respect to the fast time plus a fluctuation about this average. Then, substituting into (25), using (31) and (32), and gathering terms with the same power of ϵ gives at $O(\epsilon^{-1})$

$$\frac{\partial \tilde{S}}{\partial \tau} + \boldsymbol{v} \cdot \nabla_y \tilde{S} + \boldsymbol{v} \cdot \nabla_y \hat{S} = 0. \tag{95}$$

If S_ϵ is initially smooth, then $\boldsymbol{v} \cdot \nabla_y \hat{S}$ will be zero and $\tilde{S} = 0$. Hence $\tilde{S}$ will be identically zero for all subsequent times, and hence no fast time scales appear in the solution. Note that this is also the case if $\hat{S} \in \mathcal{N}$ initially (this provides the constraint on the initial form of the fluctuations S'). If $\hat{S}$ has any component in $\mathcal{W}$, then $\tilde{S}$ will be nonzero, and hence the fast time scale appears. In our problems, the initial saturation will always be smooth. However, in the course of numerical computations, at steps beyond the first, we are in effect solving (25) with oscillatory initial data, and due to numerical errors this may not exactly lie in the space $\mathcal{N}$. Therefore, it is important to show that if this is the case, these errors do not grow.

To show that this is indeed the case, we need to show that S_1 remains bounded as $\tau \to \infty$. To do this, we derive the equation for S_1. Taking (93) as our *given* equation for S', we subtract it from the fluctuation equation (80) to obtain, upon simplification,

$$\begin{aligned} \frac{\partial S_1}{\partial \tau} + f_S \boldsymbol{v} \cdot \nabla_y S_1 = &- \mathcal{Q}(\boldsymbol{v}') \cdot \left[\nabla_x (\overline{f} + f')\right] - (\overline{\boldsymbol{v}} + \mathcal{P}(\mathbf{v}')) \cdot \mathcal{Q}(\nabla_x f') \\ &+ \mathcal{P}\left(\mathcal{Q}(\boldsymbol{v}') \cdot \mathcal{Q}\left(\nabla_x f'\right)\right) - \mathcal{Q}\left(\frac{\partial S'}{\partial t}\right). \end{aligned} \tag{96}$$

If we project this onto the streamlines defined by $f_S \boldsymbol{v}$, then the left-hand side becomes a total derivative. To show that S_1 remains bounded, we must estimate how fast the terms on the right-hand side decay along the streamline. Suppose first that the streamlines reconnect. Then, by Lemma 3.9, since the projection $\mathcal{P}$ is invariant if we multiply $\boldsymbol{v}$ by $g \in \mathcal{N}$, the integral of the right-hand side over one such period is exactly $P\mathcal{P}(RHS)$, where as before P is the length of the path the streamlines traverse before reconnecting. Taking the $\mathcal{P}$ projection of these terms and using the fact that $\mathcal{P}(\mathcal{Q}(u)) = 0$ and the other properties of $\mathcal{P}$ these become

$$-\mathcal{P}\left(\mathcal{Q}(\mathbf{v}') \cdot \nabla_x f'\right) - \mathcal{P}\left(\mathcal{P}(\boldsymbol{v}') \cdot \mathcal{Q}(\nabla_x f')\right) + \mathcal{P}\left(\mathcal{Q}(\boldsymbol{v}') \cdot \mathcal{Q}\left(\nabla_x f'\right)\right). \tag{97}$$

Using Lemma 3.8 the second term is zero. Then, combining the other terms

$$\begin{aligned} -\mathcal{P}\left(\mathcal{Q}(\mathbf{v}') \cdot \nabla_x f'\right) + \mathcal{P}\left(\mathcal{Q}(\boldsymbol{v}') \cdot \mathcal{Q}\left(\nabla_x f'\right)\right) &= \mathcal{P}\left[\mathcal{Q}(\boldsymbol{v}') \cdot \left(\nabla_x f' - \mathcal{Q}\left(\nabla_x f'\right)\right)\right] \\ &= \mathcal{P}\left[\mathcal{Q}(\boldsymbol{v}') \cdot \mathcal{P}(\nabla_x f')\right] \\ &= \mathcal{P}\left(\mathcal{Q}(\boldsymbol{v}')\right) \cdot \mathcal{P}(\nabla_x f') \\ &= 0. \end{aligned}$$

Thus, $P\mathcal{P}(RHS) = 0$. Hence S_1 is periodic and bounded over this interval P.

If the streamlines do not reconnect, then we still have that the average of the right-hand side terms approach zero as $T \to \infty$. Thus, we have $S_1(T)/T \to 0$ as $T \to \infty$, which shows that S_1 at least grows sublinearly.

4. Numerical implementation. In this section, we describe how to take the analysis given in the previous sections and translate this into a scheme for computing upscaled numerical solutions to our two-phase flow problem.

The results of the analysis given in section 3 lead to the upscaled equations (15) for the pressure equation and (92) for the saturation. As mentioned, both retain the original character of the problem (3), (4); i.e., the upscaled pressure equation remains elliptic and the upscaled saturation equation remains hyperbolic. From now on, when we refer to the "saturation" equation we mean the upscaled equation (92) and when we refer to the "pressure" equation we mean (15). The multiple scale analysis was sequential, in that period fluctuations in the permeability give rise to period fluctuations in the velocity and this then gives rise to periodic fluctuations in the saturation. The numerical method we employ is similarly sequential. We first solve the pressure equation (15) via an implicit, elliptic method and then use the resulting velocity field to explicitly update the saturation (92). These equations are solved on *coarse* grids. However, as was noted, in both equations we need to compute fluctuating quantities (from (16) for the pressure equation and (93) and the velocity fluctuations for the saturation equation). Thus, in addition to the coarse grid, we also define subgrids within each of the coarse grid cells that enable us to compute these quantities.

4.1. Numerical scheme for the saturation equation. Recall our set of equations for the evolution of the average and fluctuation of the saturation

$$\frac{\partial \overline{S}}{\partial t} + \overline{\boldsymbol{v}} \cdot \nabla_x \overline{f} = -\nabla_x \cdot \overline{\boldsymbol{v}' f'}, \tag{98}$$

$$\frac{\partial S'}{\partial t} + (\overline{\boldsymbol{v}} + \mathcal{P}(\boldsymbol{v}')) \cdot \nabla_x f' + \mathcal{P}(\boldsymbol{v}') \cdot \nabla_x \overline{f} = \nabla_x \cdot \overline{\boldsymbol{v}' f'} + G(\boldsymbol{x}, \boldsymbol{y}, t), \tag{99}$$

$\overline{S}$ being the spatial average of the multiscale solution S_ϵ (the solution of our original system (3), (4)) and S' the $O(1)$ fluctuation about this average. The terms are G given by (94) and note that we have now moved the small-scale large-scale interaction terms $\nabla_x \cdot \overline{\boldsymbol{v}' f'}$ to the right-hand side of both equations, where they are now treated as source terms. $\overline{\boldsymbol{v}}$ and $\boldsymbol{v}'$ are the average and fluctuation of the velocity field. Note that the fluctuation equation (99) has dependence on the fast spatial variable $\boldsymbol{y}$ but that this appears only as a parameter. The strategy we use for solving such a system when coupled with the source terms is a fractional-step method, as described in [23].

For this hyperbolic part, we can take advantage of the well-developed theory that exists for solving such systems numerically. Since the fluctuations in the saturation will develop steep gradients and shocks, consistent with the original scalar problem, the numerical scheme must be able to handle these features of the solution. Finite-volume schemes are perfectly suited to handle such issues, and we choose to use the class of schemes known as wave-propagation methods, developed by LeVeque [23]. These are implemented via the freely available package CLAWPACK [22]. The updating of the source terms is done using a second-order Runge–Kutta method. We refer the reader to [27] for more discussion on the implementation details.

In above equations the term $\nabla_x \cdot \overline{\boldsymbol{v}' f'}$ is important, as it captures the interaction of the small-scale features on the large scale. It is therefore worth mentioning how

this term is treated numerically. At each time step the average $\overline{\boldsymbol{v}'f'}$ is computed on the coarse grid using the subgrid solutions for $\boldsymbol{v}'$ and f' at the previous time step. We then perform finite differencing of this to obtain an approximation for $\nabla_x \cdot \overline{\boldsymbol{v}'f'}$. It was found that upwind differencing is needed for stability (upwind with respect to the coarse grid velocity $\overline{\boldsymbol{v}}$); i.e., for $\left(\overline{\boldsymbol{v}'f'}\right)_{x_1}$, if $\overline{\boldsymbol{v}}_1 > 0$, then we use the approximation

$$\left(\overline{\boldsymbol{v}'f'}\right)_{x_1} \approx \frac{\left(\overline{\boldsymbol{v}'f'}\right)_{i,j} - \left(\overline{\boldsymbol{v}'f'}\right)_{i-1,j}}{\Delta x_1}; \tag{100}$$

otherwise if $\overline{\boldsymbol{v}}_1 < 0$, then we use

$$\left(\overline{\boldsymbol{v}'f'}\right)_{x_1} \approx \frac{\left(\overline{\boldsymbol{v}'f'}\right)_{i+1,j} - \left(\overline{\boldsymbol{v}'f'}\right)_{i,j}}{\Delta x_1}. \tag{101}$$

The x_2-derivatives are approximated in a corresponding manner. Despite being first-order approximations, these were found to be adequate. When second-order central difference approximations were used, spurious oscillations formed in the solution.

4.1.1. Computation of streamline projection. From the section on multiscale analysis, we see that the streamline projection $\mathcal{P}$ is a fundamental component of the upscaling scheme, since it eliminates the fast time dependence. In numerically computing this quantity we may choose to use either (41) and Corollary 3.1, or (73) and (74). While the second of these is useful for interpretation, it was found that using this form to numerically compute the projection was cumbersome. Thus, to compute the projections $\mathcal{P}$ and $\mathcal{Q}$ we use (41) and Corollary 3.1. Recall that in order to obtain $\mathcal{Q}(u)$ we must solve

$$\nabla_y \cdot (A \nabla_y \theta) = \boldsymbol{v} \cdot \nabla_y u \tag{102}$$

with periodic boundary conditions, where A is the 2×2 matrix with components $A_{ij} = v_i v_j$. Then, $\mathcal{Q}(u) = \boldsymbol{v} \cdot \nabla_y \theta$. $\mathcal{P}(u)$ is then obtained via $\mathcal{P}(u) = u - \mathcal{Q}(u)$. Equation (102) is degenerate because A is singular, having eigenvalues 0 and $v_1^2 + v_2^2$. Because of this, solving this equation is more difficult than a standard elliptic equation, where most solution methods rely on A being positive-definite. For example, we had no success in using finite element methods to try to solve (102) numerically. As noted in section 3, the solution of (102) is unique only up to a function in $\mathcal{N}$.

Because of the difficulties associated with A being singular, to solve (102) we instead consider the related equation

$$\frac{\partial g}{\partial \mu} = \nabla_y \cdot (A \nabla_y g) - \boldsymbol{v} \cdot \nabla_y u \tag{103}$$

with periodic boundary conditions, where μ is an "artificial time." The steady state solution of this equation is clearly a solution of (102). Thus, the idea is to solve (103) to a steady state using time stepping, starting from an initial guess of the solution. We do this by employing a semi-implicit discretization,

$$\frac{g^{n+1} - g^n}{\Delta \mu} = \alpha \nabla^2 g^{n+1} + \nabla_y \cdot (A \nabla_y g^n) - \alpha \nabla^2 g^n - \boldsymbol{v} \cdot \nabla_y u, \tag{104}$$

where α is a constant, chosen to improve the rate of convergence to the steady state. Rearranging terms in this equation gives

$$\left(1 - \alpha \Delta \mu \nabla^2\right) g^{n+1} = \left(1 - \alpha \Delta \mu \nabla^2\right) g^n + \Delta \mu \nabla_y \cdot (A \nabla_y g^n) - \Delta \mu \boldsymbol{v} \cdot \nabla_y u \tag{105}$$

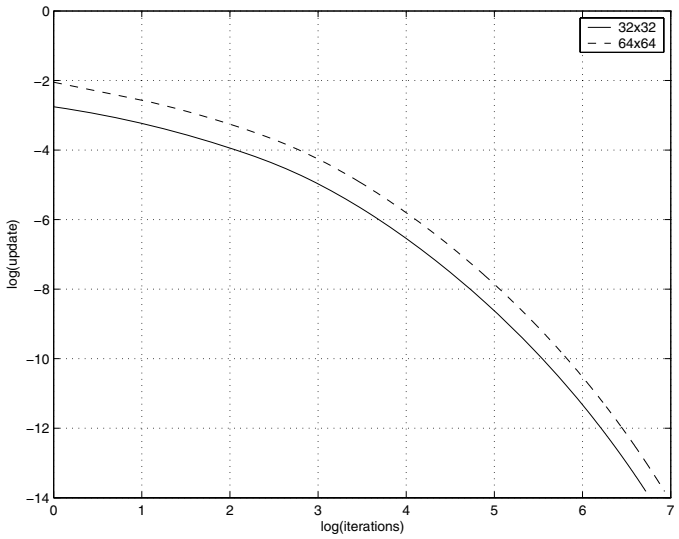

FIG. 1. *Log-log convergence plot of l_2-norm of the update in the projection computations, using 32×32 and 64×64 grids.*

so that at each time step, we solve a constant coefficient elliptic equation for g^{n+1}. This is easily accomplished on a uniform Cartesian grid and fast Fourier transforms (FFTs). The grid corresponds exactly to the subgrid for $\boldsymbol{y}$. In addition, all derivatives were calculated using the FFT. This method of solution is similar to that used by Ceniceros and Hou [5].

Using (105) with $\Delta\mu = 1/K$ we marched to a steady state, which was when $\| g^{n+1} - g^n \|_{l_2}$ was less than a specified tolerance (usually 10^{-6}). The initial guess was taken simply to be $g = 0$ everywhere (note that it would have been better to use the g computed from the previous time step of the hyperbolic solver but that this would have required too much memory). The convergence rate was generally found to be rather slow, particularly for velocity fields $\boldsymbol{v}$ with complicated features. Several experiments were done to try to determine an optimal value for α that would give both a decent convergence rate and also be robust enough so that the scheme converged over a wide range of velocity fields. The value of α that seemed to work best was

$$\alpha \approx 0.7 \max_{Y} \sqrt{v_1^2 + v_2^2}, \tag{106}$$

with the maximum taken over the subgrid in each coarse cell (i.e., a different α is used in each coarse grid cell). Figure 1 shows the log-log plot of the convergence rate of the scheme for the particular velocity field given by (107) and (108) with $x_1 = 0.5$, $x_2 = 0.5$ and when taking the projection of the v_1' component of it. These are computed using 32×32 and 64×64 points for the subgrid. The important property of the projection is that it returns a function $p \in \mathcal{N}$, i.e., with $\boldsymbol{v} \cdot \nabla_y p = 0$. Our numerical results show that to within a reasonable degree, our computed p lies in $\mathcal{N}$.

4.1.2. Consistency and convergence of our scheme for the saturation equation. It is important that we evaluate each part of the numerical scheme separately to ensure that it behaves as our analysis predicts. Therefore, since we have

described the numerical implementation of the hyperbolic part of the scheme, we present some results that demonstrate that the method works. We compare the results for our upscaling scheme with resolved computations, computing error norms.

To avoid the issues involved in computing the velocity field numerically, we prescribe an analytical form for the velocity. We choose one such that the divergence-free property holds and also has fluctuations with a periodic structure. Any such velocity should be "realistic" in that it should mimic features that are typically seen in porous media flows. For instance, the fluctuations should be $O(1)$ and have a sufficiently complicated structure so that the streamline projection is not trivial to compute, e.g., shear flows. The following velocity field provides a reasonable model upon which to test the scheme:

$$\overline{\boldsymbol{v}}(\boldsymbol{x}) = (4 + \cos(6\pi x_2), 0)\,, \tag{107}$$

$$\boldsymbol{v}'(\boldsymbol{x}, \boldsymbol{y}) = \frac{2}{3}\pi \sin(4(x_1 + x_2)) \cos(2\pi(y_1 + y_2))(1, -1) + (\sin(2\pi y_1), 0). \tag{108}$$

Numerical computations show that the streamlines are close to that for a shear flow, but there are small fluctuations in the vertical directions due to the multiscale velocity field.

We use the unit domain ($0 \le x_1 \le 1$ and $0 \le x_2 \le 1$) for all our computations. We need to prescribe an initial saturation for the problem. For this we use an initially smooth (i.e., with no spatial fluctuations) function S_0 given by

$$S_0 = \begin{cases} 1, & x_1 < \left(b - \frac{\delta}{4}\right), \\ \frac{1}{2}\left[1 - \sin\left(\frac{2\pi(x_1 - b)}{\delta}\right)\right], & |x_1 - b| < \frac{\delta}{4}, \\ 0, & x_1 > \left(b - \frac{\delta}{4}\right). \end{cases} \tag{109}$$

This initial saturation corresponds to a jump centered at $x_1 = b$ mollified by the parameter δ.

We perform a convergence analysis for the scheme using the setup described above. Although the velocity field is given analytically, an analytical form for the evolution saturation is hard to determine. Therefore, as is often done in the evaluation of numerical schemes for homogenization, we take well-resolved computations to be our "exact" solution. The scheme is tested with different coarse grids, which for simplicity will always be uniform with an equal number of grid blocks in the x_1- and x_2-directions. We keep the number of grid points for the cell problems always the same. By analysis similar to that described in the evaluation of the streamline projection, we determined that 32×32 grid points were sufficient to accurately compute the fluctuations.

We compare the results for both the homogenized solution, i.e., $\overline{S}$, and also $\overline{S} + S'$, which, by our multiscale analysis, should give the exact solution S_ϵ to within $O(\epsilon)$. Note that since we have prescribed the form of the velocity field analytically, the value of the small-scale parameter ϵ does not actually appear anywhere in the computations (all the evaluations for the cell problem are scaled so that ϵ does not appear explicitly). However, in comparing with the exact solution we must choose a particular value for ϵ. We choose $\epsilon = 1/128$, which is much smaller than the mesh size of the largest coarse grid. We choose this value, since it allows us to more easily reconstruct the solution $\overline{S} + S'$, which we will refer to as the "multiscale reconstruction." We do not, however, take any advantage of the fact that this ϵ is rational.

We compute solutions on the coarse grids $N \times N$, with $N = 16, 32, 64$. The "exact" solution is computed on a 2048×2048 grid. For the resolved computations,

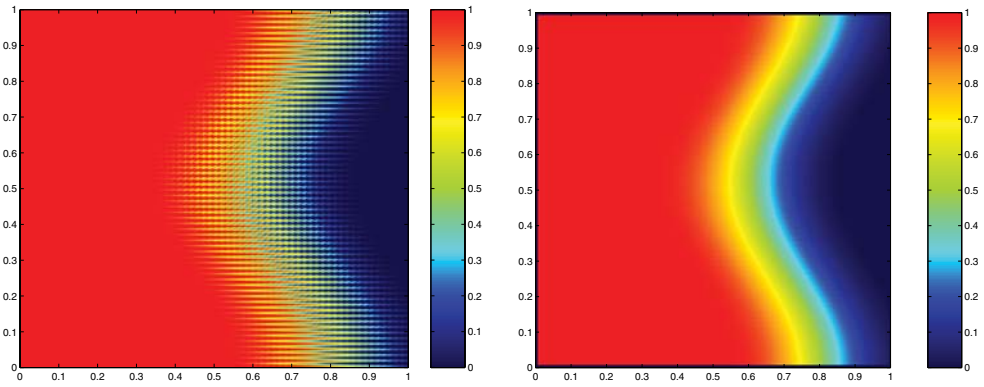

FIG. 2. *Contour plot for the "exact" solution for the saturation in the single-phase case, resolved solution, and average.*

we compute a homogenized solution by taking the numerical spatial average. For both $\overline{S}$ and $\overline{S} + S'$ we compute discrete error norms. We compute the l_2-norm and the infinity norm, which are given, respectively, by

$$\| U - U_h \|_{l^2} = \left(\sum_k \int_k (U - U_h)^2 d\boldsymbol{x} \right)^{\frac{1}{2}}, \qquad \| U - U_h \|_\infty = \max_k |U - U_h|,$$

where k is a grid block and K is the set of grid blocks over the domain. Here we take U to be the resolved saturation (or average) and U_h the corresponding saturation computed via our upscaling scheme. For the "exact" average saturation we compute the average of the resolved solution using a numerical quadrature, with the area of integration corresponding to exactly one oscillation cell. This was done at points corresponding to the centers of the coarse grid used in the upscaled calculations.

We first show the results for the more simple case of single-phase flow ($f(S) = S$ in the saturation equation). Figure 2 shows the resulting solution at time $t = 0.1$. This time is sufficient to allow the fluctuations in the saturation to form while maintaining the whole front to remain within the domain. From the figure we can see the saturation "fingers" that develop.

Figure 3 shows the corresponding solutions computed from our upscaling scheme. Comparing with the resolved computations we see that the scheme accurately captures the overall profile and the fluctuations. Indeed, the results on the 64×64 coarse grid appear almost identical. Figure 4 shows the average saturation, which is the quantity of most interest, on the same grids.

Tables 1 and 2 show the errors in the homogenized solution and the multiscale reconstruction for the single-phase case.

We see that the scheme is first-order accurate as expected, since the updating of the source terms is first-order.

If we ignore the interaction terms in the average equation (92), then the average saturation is not captured correctly. We investigate this numerically by comparing the average saturation contours for the upscaling method above and in the case when the interaction term $\nabla \cdot \overline{\boldsymbol{v}' f'}$ is ignored; i.e., we solve

$$\frac{\partial \overline{S}}{\partial t} + \overline{\boldsymbol{v}} \cdot \nabla_x f(\overline{S}) = 0. \tag{110}$$

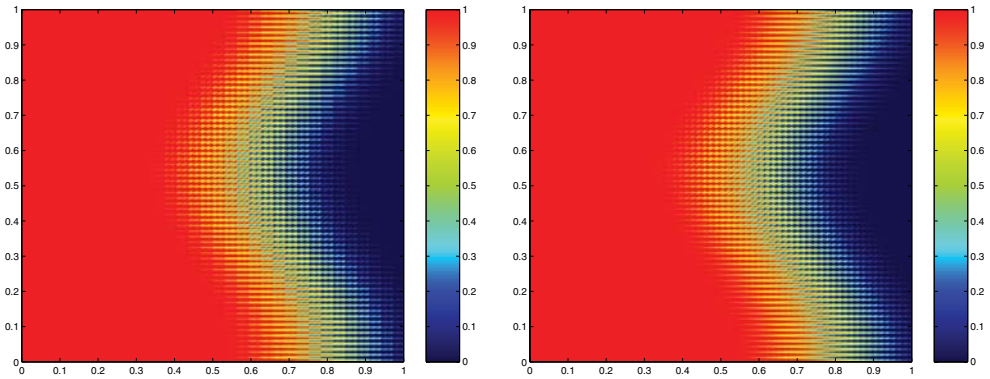

FIG. 3. *Multiscale reconstruction of the saturation from the upscaling scheme for the single-phase case using* 32×32 *and* 64×64 *coarse-grids.*

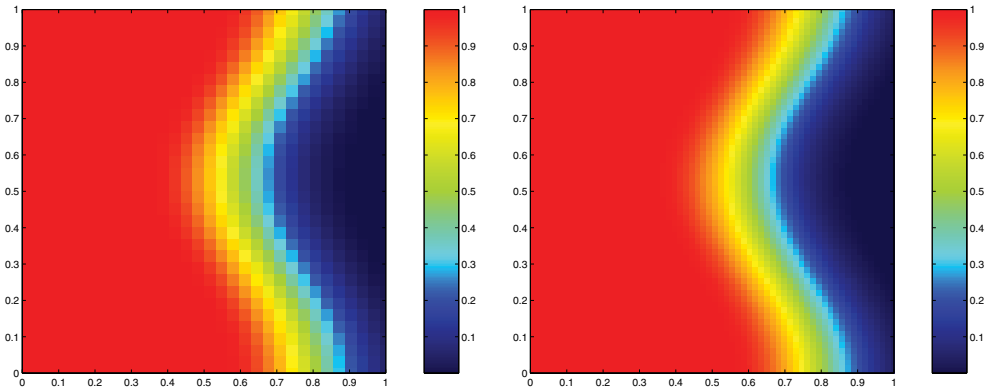

FIG. 4. *Average saturation from the upscaling scheme for the single-phase case using* 32×32 *and* 64×64 *coarse grids.*

TABLE 1
Errors in the multiscale reconstruction in the single-phase case using different grids.

N	l^2 error	Max error
16	0.0276	0.3012
32	0.0140	0.1541
64	0.0069	0.0686

TABLE 2
Errors in the homogenized solution in the single-phase case using different grids.

N	l^2 error	Max error
16	0.0144	0.0460
32	0.0070	0.0233
64	0.0034	0.0071

We show that if the interaction terms are ignored, we do not get the right amount of "spreading" of the average saturation front; see [27] for more discussion.

We next show the results for the two-phase flows. We again use the same velocity field and same initial data for the tests. In addition, we use exactly the same grids

TABLE 3
Errors in the multiscale reconstruction in the two-phase case using different grids.

N	l^2 error	Max error
16	0.0697	0.7007
32	0.0524	0.6959
64	0.0467	0.6811

TABLE 4
Errors in the homogenized solution in the two-phase case using different grids.

N	l^2 error	Max error
16	0.0723	0.0354
32	0.0433	0.0251
64	0.0275	0.0212

TABLE 5
Errors in the multiscale reconstruction in the two-phase case using different grids, before shock forms.

N	l^2 error	Max error
16	0.0184	0.1120
32	0.0095	0.0764
64	0.0049	0.0461

TABLE 6
Errors in the homogenized solution in the two-phase case using different grids, before shock forms.

N	l^2 error	Max error
16	0.0270	0.0831
32	0.0148	0.0495
64	0.0076	0.0264

for both the coarse and subgrids. Tables 3 and 4 show the errors in the solution. We again see that the upscaled calculations capture the solution well.

In this case, we see that the error convergence is less than first-order, being approximately 0.4 for the reconstructed solution and approximately 0.7 for the homogenized solution. This is due to the fact that a shock has already formed in the solution by this time, and so the formal convergence rates no longer apply. To check that the scheme has first-order rate of convergence, we computed the solution before the shock forms, at $t = 0.05$. The corresponding errors are shown in Tables 5 and 6 show clearly that the scheme is first-order.

4.2. Numerical upscaling method for the pressure/velocity equation. We now turn to the problem of developing a numerical upscaling scheme for the pressure/velocity equation (PVE) (3). The multiscale analysis of section 3.2 shows us that for permeability fields with $O(1)$ oscillations (in the fast variable $\boldsymbol{y}$) we can expect that the velocity field (needed in the saturation equation) will also have oscillations which are $O(1)$.

The goal of the upscaling scheme is of course to be able to solve (3) on a coarse grid. Moreover, in fact, we wish to use the same coarse grid that is used for the saturation scheme. Should we wish to get only the solution at coarse grid points, i.e., only the average $\overline{\boldsymbol{v}}$, then we would either look to solve the homogenized equation (15) with an approximation for the "equivalent" permeability $a^*(\boldsymbol{x}, t)$ or else use expression (16) which is valid in the case of periodic oscillations. As mentioned in the

introduction, there have been several attempts to calculate equivalent permeabilities for different flow situations. However, in our scheme for the saturation equation, we see that we need to have not only the average velocity but also the fluctuations $\boldsymbol{v}'$, e.g., in (92), where we need to evaluate the interaction term $\nabla_x \cdot \overline{\boldsymbol{v}' f'}$. Therefore, the scheme must be capable of providing both. At first this may appear a contradictory goal: we wish to upscale, i.e., solve the equation on a coarse grid, and yet be able to get fine-scale information within the same scheme. This contradiction can be resolved if we realize that may be able to somehow *interpolate* the coarse grid solution, using only locally computed quantities, to get fine-scale information within the interior of coarse grid cells. We are fortunate that such a method with this philosophy already exists and incorporating it into our scheme is just a matter of effective implementation. This method is the multiscale finite element method, which we describe below. The method is special in the sense that it can be viewed as an upscaling method, and yet it also provides a handle to fine-scale information. This latter feature is sometimes referred to as *downscaling*.

4.2.1. Multiscale finite element method. The multiscale finite element method (MsFEM) for elliptic problems is fully described in [15, 16, 13]. We will give an outline of the method and then describe the adaptations needed to use it efficiently in our scheme.

Consider our elliptic pressure equation (3),

$$-\nabla \cdot (a(\boldsymbol{x}, t)\nabla p) = f, \tag{111}$$

where, as in the section on multiscale analysis, we have written $a = \lambda(S)K$. Since a depends on the saturation it is actually time dependent. However, since we are advancing the numerical solution to (3), (4) by alternately solving each separately, we can consider t as a parameter when solving the pressure equation. In our case, the source term f will be zero everywhere unless there exist source or sinks within the domain. However, for generality in describing the method we leave it in (111). For the moment, $\boldsymbol{x}$ is used to denote a general spatial variable, rather than the coarse grid variable used above.

For the purpose of deriving the method, we first suppose that (111) holds in a domain Ω and that $p = 0$ on $\partial\Omega$. The modifications for handling inhomogeneous boundary conditions are trivial. The variational problem of (111) is then to seek $p \in H_0^1(\Omega)$ such that

$$a(p, q) = f(q) \quad \forall q \in H_0^1(\Omega), \tag{112}$$

where

$$a(p, q) = \int_\Omega a(\boldsymbol{x}) \frac{\partial q}{\partial x_i} \frac{\partial p}{\partial x_i} d\boldsymbol{x}, \tag{113}$$

$$f(q) = \int_\Omega f(\boldsymbol{x}) q(\boldsymbol{x}) d\boldsymbol{x} \tag{114}$$

(summation convention is used for repeated indices here). Since $a(\boldsymbol{x}, t)$ is bounded from below by a positive constant, the linear form $a(\cdot, \cdot)$ is elliptic and continuous, i.e.,

$$\alpha \, |q|_{1,\Omega}^2 \leq a(q, q) \quad \forall q \in H_0^1(\Omega) \tag{115}$$

and

$$|a(p,q)| \leq \beta\,|p|_{1,\Omega}\,|q|_{1,\Omega} \quad \forall q \in H_0^1(\Omega). \tag{116}$$

A *finite element* method is obtained by restricting the weak formulation (112) to a finite dimensional subspace of $H_0^1(\Omega)$. Let $\mathcal{K}^h$ be a partition of Ω of elements K with diameter less than h. In our method we will always assume that the partition consists of rectangular elements which are defined by an axiparallel rectangular mesh and with maximum edge length h. This case covers the meshes we described in the previous sections for the saturation equation. Let $\boldsymbol{x}_s \in \overline{K}$ $(s = 1, \ldots, d)$, $d = 4$, be the nodal points of K. In each element $K \in \mathcal{K}^h$, we define a set of *basis functions* $\{\phi_K^r, i = 1, \ldots, d\}$. In the traditional finite element method these basis functions would be bilinear function [3]. In MsFEM, these basis functions satisfy

$$-\nabla \cdot (a(\boldsymbol{x})\nabla \phi_K^r) = 0 \tag{117}$$

inside K. As is usual for finite element basis functions we require $\phi_K^r(\boldsymbol{x}_s) = \delta_{rs}$. Further, we need to specify the boundary conditions of ϕ_K^r for well-posedness of (117). The choice of boundary conditions on the basis functions has a strong influence on the convergence of MsFEM. For the moment we assume that the boundary conditions are linear along the boundaries of the elements, i.e., along the boundaries on which MsFEM basis functions and traditional (linear) finite element basis functions coincide.

MsFEM with these basis functions is conforming, i.e.,

$$V^h = \operatorname{span}\{\phi_K^r : i = 1, \ldots, d; K \in \mathcal{K}^h\} \subset H_0^1(\Omega) \tag{118}$$

and the approximate solution of (111) in V^h, i.e., $p^h \in V^h$, is

$$a(p^h, q) = f(q) \quad \forall q \in H_0^1(\Omega). \tag{119}$$

We can see that the only difference between MsFEM and a traditional finite element method is in the construction of the basis functions. Note that (119) is solved at the coarse grid level, with the solution p^h given at coarse grid nodes, and it is in this sense that it is an upscaling scheme.

4.2.2. Special MsFEM for the case of periodic oscillations. In the case of periodic oscillations such as those that have been considered in section 3, we may employ a variant of the MsFEM that gives a numerical two-scale solution directly, i.e., a solution of the form $p = p(\boldsymbol{x}, \boldsymbol{y})$. Recall that the basis functions in MsFEM satisfy (117) within a coarse grid cell. a is assumed to be of the form $a = a(\boldsymbol{x}, \boldsymbol{y})$ and periodic in $\boldsymbol{y}$. In exactly the same way as the pressure equation had an asymptotic expansion of the form (14), the basis functions will have an expansion of the form

$$\phi_K^r = \phi_{0,K}^r(\boldsymbol{x}) + \epsilon\phi_{1,K}^r(\boldsymbol{x}, \boldsymbol{y}) + \epsilon^2\phi_{2,K}^r(\boldsymbol{x}, \boldsymbol{y}) + O(\epsilon^3). \tag{120}$$

Using an exactly similar analysis that was used to derive the expressions (15) and (18) for p_0 and p_1 and now applied to (120) we get

$$\frac{\partial}{\partial x_i}\left(a^*(\boldsymbol{x})\frac{\partial \phi_{0,K}^r}{\partial x_i}\right) = 0 \tag{121}$$

and

$$\phi_{1,K}^r(\boldsymbol{x}, \boldsymbol{y}) = -\chi^j \frac{\partial \phi_{0,K}^r}{\partial x_j}, \tag{122}$$

where a^* is a diagonal tensor with

$$a^*_{ij}(\boldsymbol{x}) = \frac{1}{|Y|}\int_Y a(\boldsymbol{x},\boldsymbol{y})\left(1-\frac{\partial\chi^j}{\partial y_i}\right)d\boldsymbol{y} \tag{123}$$

and χ^j satisfies

$$\frac{\partial}{\partial y_i}\left(a(\boldsymbol{x},\boldsymbol{y})\frac{\partial\chi^j}{\partial x_i}\right) = \frac{\partial a}{\partial y_j} \tag{124}$$

with periodic boundary conditions.

The coarse grid will always have sufficient resolution so that the elements in $a^*(\boldsymbol{x})$ can be approximated by constants throughout a coarse grid cell K. Thus, (121) with linear boundary conditions will have solutions that correspond to the standard bilinear basis functions. That is, the $\phi^r_{0,K}$ are the standard bilinear basis functions. Then, we take

$$\phi^r_K = \phi^r_{0,K} + \epsilon\phi^r_{1,K} \tag{125}$$

$$= \phi^r_{0,K} - \epsilon\chi^j\frac{\partial\phi^r_{0,K}}{\partial x_j}, \tag{126}$$

which gives the basis functions to within $O(\epsilon^2)$. To determine the basis functions in all the coarse grid blocks, we need to solve (124) within each to obtain χ^j, $j = 1, 2$, and then use these in (126).

Once the solution for the pressure has been obtained at coarse grid points, via the usual construction of the stiffness matrix and solving the resulting linear equations, we can reconstruct the two-scale pressure within each cell using

$$p = \sum_r^d p^h_r\phi^r_K \tag{127}$$

$$= \sum_r^d p^h_r\left(\phi^r_{0,K} - \epsilon\chi^j\frac{\partial\phi^r_{0,K}}{\partial y_j}\right) + O(\epsilon^2). \tag{128}$$

We call this a two-scale numerical solution since it has variation with respect to the coarse grid (each p^h_r is given at coarse grid node) and variation within the cell (χ^j is varying as a function of $\boldsymbol{y}$ inside the cell). We can prove the convergence of this MsFEM, and this is given in [27] along with numerical examples. To obtain the two-scale velocity field for use in our scheme for the saturation equation, we use Darcy's law

$$\boldsymbol{v} = -a(\boldsymbol{x},\boldsymbol{y})\nabla p \tag{129}$$

$$= -a(\boldsymbol{x},\boldsymbol{y})\sum_r^d p^h_r\left(\frac{\partial\phi^r_{0,K}}{\partial x_i} - \frac{\partial\chi^j}{\partial y_i}\frac{\partial\phi^r_{0,K}}{\partial x_j}\right) + O(\epsilon). \tag{130}$$

We compute $\boldsymbol{v}$ at the center of each coarse grid cell using (130) and then take the average of this to obtain $\overline{\boldsymbol{v}}$ and $\boldsymbol{v}'$, which are then used in the scheme for the saturation equation. Note that χ^j and hence $\boldsymbol{v}'$ are solved for on exactly the subgrid described in the previous sections for the saturation equation, and the average velocity is computed as a cell-centered quantity on the coarse grid.

The only disadvantage to using a finite element method in solving the pressure equation is that in the divergence-free property of the velocity field (24), in particular, neither $\nabla_x \cdot \overline{\boldsymbol{v}} = 0$ nor $\nabla_x \cdot \boldsymbol{v}' = 0$ is explicitly enforced (note that $\nabla_y \cdot \boldsymbol{v}' = 0$ by construction). Thus, the resulting velocity fields are not exactly divergence-free. This was generally not found to be a problem for our computations since the velocity field is used in the upscaled equations. When MsFEM is used for the velocity field in (25) it was found that it gave poor results for long time simulations [7, 19]. To overcome these problems, a mixed MsFEM was introduced in [7], and in [19] a multiscale finite volume method was introduced. In the section on numerical results we show that the violation of the divergence-free property is not significant for our computations.

Once the basis functions have been solved for, the solution at the coarse grid is extremely cheap. However, the construction of the basis functions is relatively expensive. Since we will be solving the pressure equation at each time step, it is worth discussing an efficient implementation of the method as it applies to our problem. In principal, since a depends on the saturation, we need to update the basis functions at each time step. The crucial observation is that for many regions, the saturation will be evolving slowly, and therefore it is not necessary to update the basis functions in these regions [20]. We can selectively choose which basis functions to update based upon how much the saturation within the cell has changed. An obvious region where basis functions would need to be updated often is near the oil-water front. Regions ahead of this front, where the water saturation is zero, would need no updating, and regions behind, where the saturation is evolving more slowly, would need updating only at less frequent intervals.

4.3. Extension to nonperiodic problems. In the multiscale analysis so far we have assumed that all small-scale fluctuations are periodic with respect to the fast variable $\boldsymbol{y}$. However, this is clearly a restrictive assumption that will not hold for realistic permeabilities. Nevertheless, the assumption is an integral part of our framework, and so we restrict our attention to permeabilities with two distinct length scales for which the fluctuations can be well approximated as being locally periodic. Given such a permeabililty, the method used will give us a permeability which approximates the original and also has periodic oscillations. In [18], a reparameterization technique has been introduced to prepare a general nonperiodic medium in a form of two-scale structure formally. In order to apply the technique in [18], we need to extend the porous media outside the computational domain by multiplying an appropriate cut-off function. Using this technique, we can apply the multiscale analysis developed earlier to general multiscale media.

For the moment we assume that our permeability $K(\boldsymbol{x})$ is a periodic function on a unit square $[0,1]\times[0,1]$, i.e., our whole domain. We expand K into its Fourier series

$$K = \sum_{\boldsymbol{r}\in Z^2} \hat{K}(\boldsymbol{r}) \exp(2\pi i \boldsymbol{r}\cdot\boldsymbol{x}), \tag{131}$$

$i = \sqrt{-1}$, $\boldsymbol{r} = (s_1, s_2)$. Choose $0 < \epsilon = 1/E < 1$ as the reference wavelength, with E the integer. Let

$$\Lambda_E = \left\{ \boldsymbol{r}; |s_j| \le \frac{E}{2}, 1 \le j \le 2 \right\}, \qquad \Lambda'_E = Z^2 - \Lambda_E. \tag{132}$$

Then,

$$K = K^{(l)} + K^{(s)}, \tag{133}$$

where

$$K^{(l)} = \sum_{\boldsymbol{r}\in\Lambda_E} \hat{K}(\boldsymbol{r}) \exp(2\pi i \boldsymbol{r}\cdot\boldsymbol{x}), \tag{134}$$

$$K^{(s)} = \sum_{\boldsymbol{r}\in\Lambda'_E} \hat{K}(\boldsymbol{r}) \exp(2\pi i \boldsymbol{r}\cdot\boldsymbol{x}). \tag{135}$$

Clearly, the component $K^{(l)}$ corresponds to the large-scale permeability, and $K^{(s)}$ corresponds to the small-scale permeability field. Here the superscripts s and l stand for small scales and large scales, respectively. For each $\boldsymbol{r}$, write

$$\boldsymbol{r} = E\boldsymbol{r}^{(s)} + \boldsymbol{r}^{(l)}. \tag{136}$$

Based on this, further decompose $K^{(s)}$ as

$$K^{(s)} = \sum_{\boldsymbol{r}\in\Lambda'_E} \hat{K}(\boldsymbol{r}) \exp(2\pi i \boldsymbol{r}\cdot\boldsymbol{x}) \tag{137}$$

$$= \sum_{E\boldsymbol{r}^{(s)}+\boldsymbol{r}^{(l)}\in\Lambda'_E} \hat{K}(E\boldsymbol{r}^{(s)}+\boldsymbol{r}) \exp(2\pi i (E\boldsymbol{r}^{(s)}+\boldsymbol{r})\cdot\boldsymbol{x}) \tag{138}$$

$$= \sum_{\boldsymbol{r}\neq 0} \left(\sum_{\boldsymbol{r}'\in\Lambda_E} \hat{K}(E\boldsymbol{r}+\boldsymbol{r}') \exp(2\pi i \boldsymbol{r}'\cdot\boldsymbol{x}) \right) \exp(2\pi i \boldsymbol{r}\cdot E\boldsymbol{x}) \tag{139}$$

$$= \sum_{\boldsymbol{r}\neq 0} \hat{K}^{(s)}(\boldsymbol{r},\boldsymbol{x}) \exp\left(2\pi i \boldsymbol{r}\cdot\frac{\boldsymbol{x}}{\epsilon}\right) \tag{140}$$

$$= K^{(s)}\left(\boldsymbol{x},\frac{\boldsymbol{x}}{\epsilon}\right), \tag{141}$$

where the coefficient $\hat{K}^{(s)}(\boldsymbol{r},\boldsymbol{x})$ contains Fourier modes lower than $E/2$ only. Thus, we can decompose a periodic function formally into a two-scale function with periodic structure:

$$K = K^{(l)}(\boldsymbol{x}) + K^{(s)}\left(\boldsymbol{x},\frac{\boldsymbol{x}}{\epsilon}\right). \tag{142}$$

More generally, by using a partition of unity, i.e., for a family of smooth cut-off functions $\{\phi_j\}_{j=1}^J$ such that

$$\phi_j \in C_0^1([0,1]^2), \tag{143}$$

$$0 \le \phi_j \le 1, \tag{144}$$

$$\sum_{j=1}^{J} \phi_j = 1, \tag{145}$$

we can decompose K as

$$K = \sum_{j=1}^{J} \phi_j K \equiv \sum_{j=1}^{J} K_j. \tag{146}$$

We can then treat K_j as a periodic function and use the same method described above to decompose the function into large and small scales. Thus, we can describe the given permeability K in the generic form

$$K = K^{(l)}(\boldsymbol{x}) + K^{(s)}(\boldsymbol{x},\boldsymbol{y}), \tag{147}$$

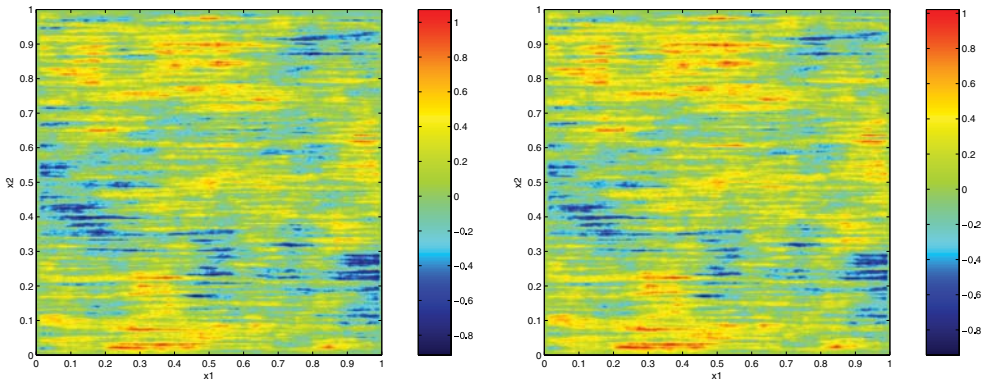

FIG. 5. *Original log permeability (left) and "reparametrized" log permeability (right) for a layered case.*

where $K^{(s)}(\boldsymbol{x}, \boldsymbol{y})$ is a periodic function of period 1 in $\boldsymbol{y}$. We can use a coarse grid with size H to resolve low frequency components of wavelength larger than ϵ and use a fine grid with size h to resolve high frequency components of wavelength smaller than ϵ. With this form for the permeability we can now apply our multiscale method for upscaling. To eliminate problems of edge effects from applying the partition of unity, we use an oversampling method. In this case, the original permeability is extended to a slightly larger domain, and the method is then applied to that domain.

We now demonstrate the ability of the reparameterization technique to capture the fluctuations correctly. We take an example permeability and apply the reparameterization technique to it. Since the permeability is a strictly positive quantity, i.e., $K > 0$ throughout the domain, we find it better to apply the method to the log of the permeability, i.e., to $u = \log(K)$. By applying it to this and then taking the exponential, we are guaranteed that the resulting approximation is also strictly positive.

To demonstrate the method we show some results for two different types of permeability. The original permeability is shown in the left plot of Figure 5. This permeability was generated using the GSLIB package on a 256×256 uniform grid. This is then interpolated (bilinear interpolation) to give a 1024×1024 permeability. The interpolation is done because the variation in the original permeability is very strong and even on a 256×256 grid can appear discontinuous as one crosses the layers of high/low permeability. With this new permeability the reparameterization method is then applied, and the resulting reconstruction is shown in the right plot of Figure 5. For this, the cut-off wavelength was $\epsilon = 1/32$. Each periodic wave was reconstructed using a 16×16 subgrid. As can be seen from the plots, the reconstruction is very close to the original permeability. Statistics for the original and reconstruction are shown in Table 7. The ratio of the correlation lengths in the horizontal and vertical directions is $l_x/l_y = 20$.

In Figure 6 we show a close-up view of corresponding regions for the original and reparametrized permeability. In the reparametrized permeability, one can see the edges of the cells over which we force the fluctuations to be periodic. Most of the features of the original permeability are retained, even at this scale. (Note that the color scheme in the close-up images is slightly different than that of the original permeability field images.)

TABLE 7
Statistics for the original and reconstructed log permeability in the layered case.

	Original	Reparametrized
Max	1.074	1.022
Min	-0.914	-0.943
Mean	0.0693	0.0693
Variance	0.0642	0.0639
l_2 error	–	0.05

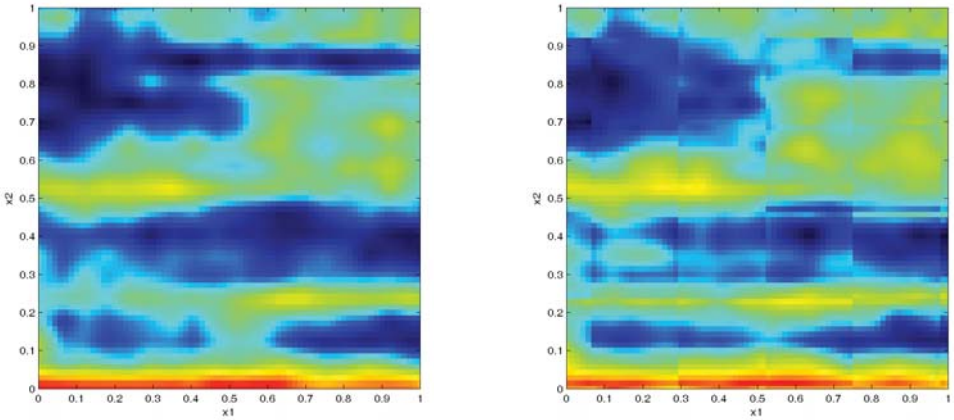

FIG. 6. *A close view of the same region for the original (left) and "reparametrized" log permeability (right).*

Note that the heterogeneity in the permeability field is not particularly large. The reason for this is that the streamline projection we employ is not very robust and fails to converge for more heterogeneous permeabilities. This is a technical difficulty, and it does not reflect the robustness of the proposed multiscale framework. We are currently exploring a different iterative strategy to improve the robustness of the streamline projection method so that it can handle permeability with realistic variances. As such the current implementation is more a demonstration of concept rather than a finished product.

5. Numerical results. In this section we present numerical results for the scheme proposed in the previous section. We first demonstrate that the scheme is first-order accurate in capturing the average saturation for the single-phase case for periodic permeabilities. We perform simulations in much the same manner as that done in section 4.1.2. In addition we now specify the boundary conditions for the pressure equation as follows:

- The two ends aligned in the horizontal direction will have zero flux condition, i.e., $\boldsymbol{v} \cdot \boldsymbol{n} = 0$, where $\boldsymbol{n}$ is the outward pointing normal.
- The two other sides will have prescribed pressures, $p = 1$ at $x_1 = 0$ and $p = 0$ at $x_1 = 1$.
- The main flow will be in the positive x_1-direction.

The resulting flow model is sometimes referred to as the "core-plug" model.

We find that our upscaling scheme very accurately computes the fractional flow curves given by (8).

TABLE 8
Errors in the multiscale reconstruction in the single-phase case using different grids.

N	l^2 error	Max error
16	0.0780	0.3725
32	0.0556	0.2793
64	0.0460	0.2239

TABLE 9
Errors in the homogenized in the single-phase case using different grids.

N	l^2 error	Max error
16	0.0745	0.2204
32	0.0419	0.1155
64	0.0215	0.0595

5.1. Periodic permeability field. To demonstrate that our method converges, we test the case where the permeability is a prescribed two-scale function. We do this for the single-phase using an analysis similar to that given in section 4.1.2. We do not use the two-phase results here, since the shock formation in that case reduces our ability to analyze the formal convergence rate of the scheme. We use only the core-plug model boundary conditions in this case.

To test, we prescribe a permeability field with fast periodic oscillations. We use

$$K(\boldsymbol{x},\boldsymbol{y}) = 15x_2(1.0-x_2) + \frac{2+P(x_1,x_2)\sin(2\pi y_1)}{2+P(x_1,x_2)\cos(2\pi y_2)} + \frac{2+\sin(2\pi y_2)}{2+P(x_1,x_2)\cos(2\pi y_1)}, \tag{148}$$

where

$$P(\boldsymbol{x}) = 1 + \frac{1}{2}\cos(\pi x_1)\cos(2\pi x_2). \tag{149}$$

We set the small-scale parameter $\epsilon = 1/64$. The permeability has rapid oscillations in the horizontal and vertical directions, with the magnitude of the oscillations greatest in the center. A similar model for the permeability was used in [15] in testing the convergence of MsFEM.

Since the pressure is uncoupled from the saturation in the single-phase case, we need only solve for this once at the start of the simulation. The first test we perform is to check the convergence for the saturation as the number of coarse grid points is increased. We do this in the same manner as that used in section 4.1.2 when we tested the scheme for the saturation separately, i.e., by comparing the results with resolved calculations for different coarse grid. Again, we use 16×16, 32×32, and 64×64 coarse grids. We keep the subgrids the same in each of these cases, using 32×32 subgrid points. The initial data for the saturation is given by (109). We evolve the saturation up until time $t = 0.1$ and then compute the l^2-and infinity norms of the error in the multiscale reconstruction and the average. Table 9 shows that our scheme has first-order rate convergence for the average saturation. Tables 8 and 10 show the errors in the multiscale reconstruction of the saturation and the velocity field, respectively.

5.2. Nonperiodic examples. We now apply all the preceding numerical methods for the upscaling problem to a case where the permeability field is non-periodic. We apply the reparameterization technique to the permeability fields shown in Figure 5 for one-phase and two-phase computations. As before, we compare the

TABLE 10
Errors in the velocity field in the single-phase case using different grids.

N	l^2 error	Max error
16	0.2098	0.4014
32	0.1216	0.2416
64	0.0655	0.1636

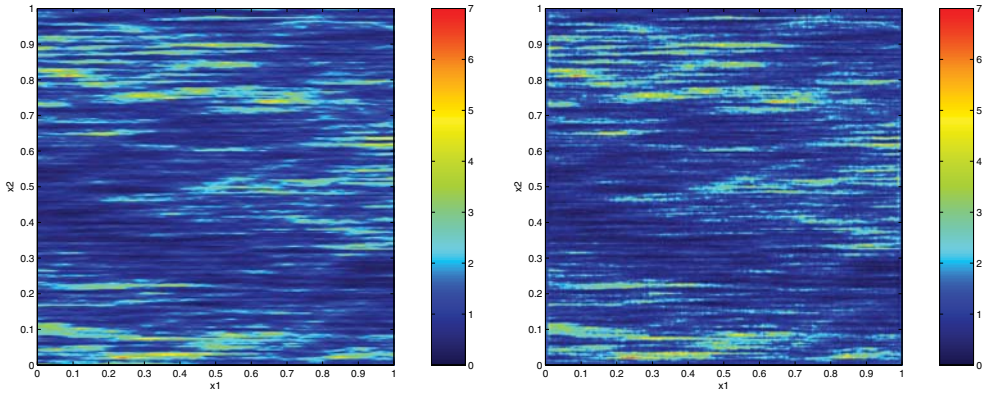

FIG. 7. *Comparison of the horizontal components of the velocity field computed using resolved scheme (left) and MsFEM (right).*

resulting solutions for the average saturation with those computed using resolved calculations. In this case, we cannot hope to obtain the same kind of convergence rates that we obtained in the previous sections where all the fluctuations had a definite periodic structure. Therefore, as a measure of accuracy, we compute the fractional flow curves that were described in section 2, given by (8). As mentioned in that section, this is a feature of interest to engineers when evaluating a reservoir simulation, and any upscaling scheme should aim to reproduce this accurately.

For the tests we use the same boundary conditions and initial data as those used in section 4.1.2. We use the same permeability field as before, with statistics given in Table 7. To use the special MsFEM, we apply the reparametrization to the permeability field before using it for our upscaling scheme. The resolved solutions are always computed using the original (no reparametrization) permeability field.

5.2.1. Single-phase results. For the resolved computations, we use a 1024×1024 grid which was found to be sufficient to fully resolve flow features. For the upscaled computations, including the permeability reparameterization, we use a 64×64 coarse grid with 16×16 subgrid points. This configuration gives us a "scale-up" factor of 8 in each direction (since the average solution is given on a 64×64 grid).

We first compare the velocity fields computed from the resolved scheme and the upscaling (MsFEM) method. Figure 7 shows the horizontal (x_1) component of the velocity field as computed by the different methods. The details of the velocity are captured well, with layers computed accurately. Because of the coarser grid in the MsFEM computations, there are some slight edge effects which can be seen. Note, however, that this velocity field shown is not used directly in the upscaled computations, but rather its average and the locally periodic fluctuations are used. The average component of the horizontal velocity as computed from the resolved scheme

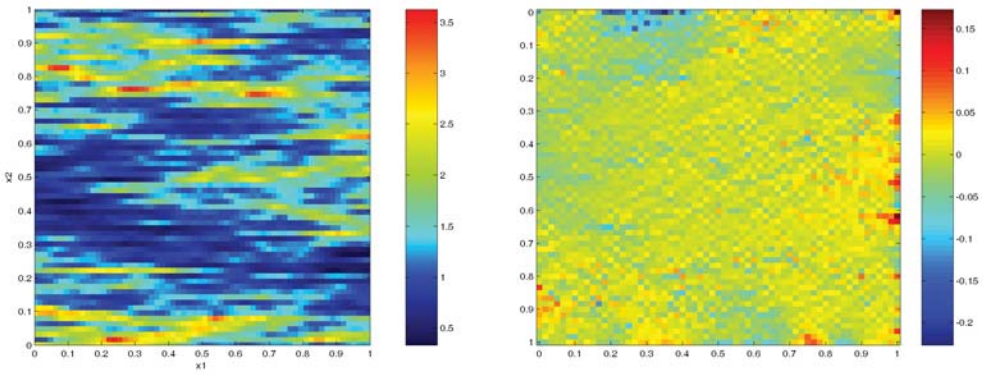

FIG. 8. *Average horizontal component of the velocity field computed using resolved scheme (left) and error in the MsFEM average velocity (right).*

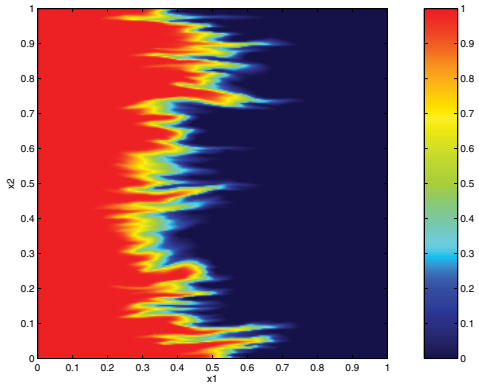

FIG. 9. *The resolved saturation at* $t = 0.17$.

is shown in Figure 8, along with the error of the MsFEM average velocity. Clearly, the MsFEM is very good at computing the average velocity.

Figure 8 shows the "exact" average saturation, computed from the resolved computations, and the average saturation when computed using the upscaling scheme.

To test how well the divergence free property holds, we compare the sum of the fluxes across all the coarse grid blocks with the outgoing flux at $x_1 = 1$. We found that the sum of fluxes was 0.00075526, whereas the outgoing flux was 1.29. Thus the nondivergence of the velocity field is quite insignificant. However, for permeability fields with more severe variations, the use of a locally conservative scheme such as mixed finite element or finite volume methods may be necessary.

The above velocity fields are now used to advance the saturation. Since the aim of the method is to accurately compute the average, we compare these when computed from the resolved calculations and the upscaling scheme at several times. Figure 9 shows the resolved calculations at time $t = 0.17$. Note the amount of "fingering" of the saturation front, which is due to the amount of layering in the permeability and velocity fields. Figure 10 shows the average saturation at this time computed from the resolved computations and upscaled scheme. From these one can see that the

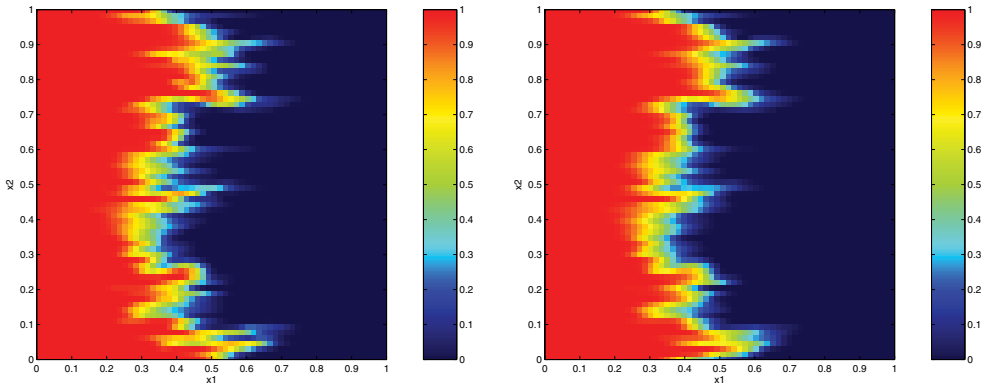

FIG. 10. *Comparison of the average saturation profiles for the single-phase case at* $t = 0.17$ *for the exact calculation (left) and upscaled scheme (right).*

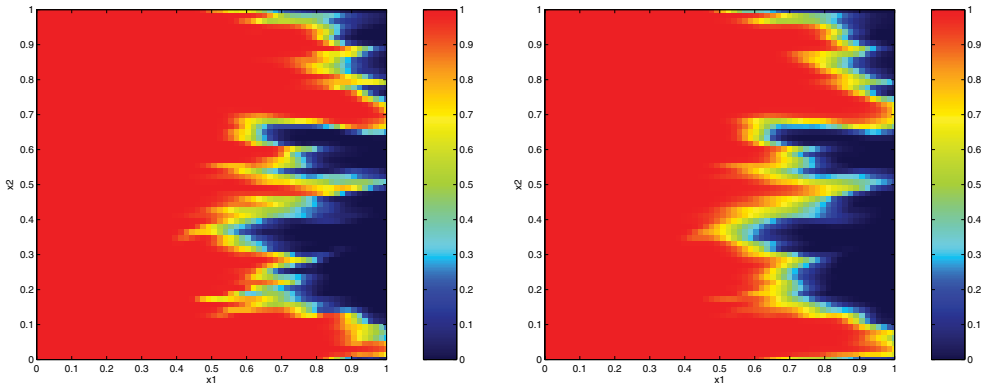

FIG. 11. *Comparison of the average saturation profiles for the single-phase case at* $t = 0.45$ *for the exact calculation (left) and upscaled scheme (right).*

upscaling scheme is accurately capturing the average.

Figure 11 shows the average saturation at time $t = 0.45$ computed from the resolved computations and upscaled scheme. Again the agreement is very good.

In addition to these we also study the case if one ignores the interaction terms when computing the average, i.e., we use (110), for the average saturation $\overline{S}$ where $\overline{\boldsymbol{v}}$ is computed using the MsFEM. We found that the average saturation is not being moved correctly in this case. This confirms that including the interaction terms is vital in computing the average correctly. It seems for this example that if the interaction terms are ignored, then the saturation is moved too slowly. Figure 12 shows the average saturation at $t = 0.3$ when the interaction terms are ignored in the computations.

Figure 13 shows the fractional flow curves computed using the resolved computations and the upscaled method. As with the saturation plots one can see that the upscaled computations accurately capture the true fractional flow. We also show that if one ignores the interaction terms in the upscaling method, then the results are much poorer. In that case, the bulk of the saturation is moved too slowly, and the fractional flow curve, labeled with "naive," is too high after the breakthrough time and remains

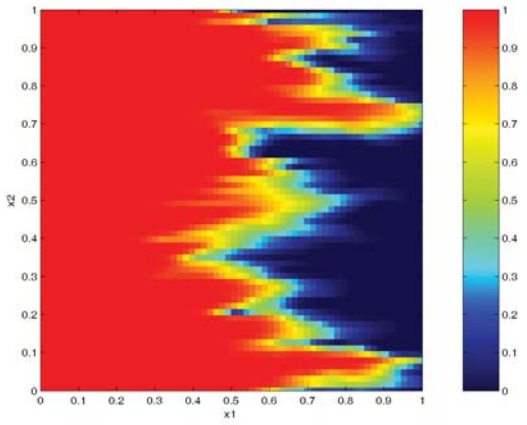

FIG. 12. *Average saturation profile at $t = 0.3$ for the naive method that ignores the subgrid interaction terms for the single-phase case.*

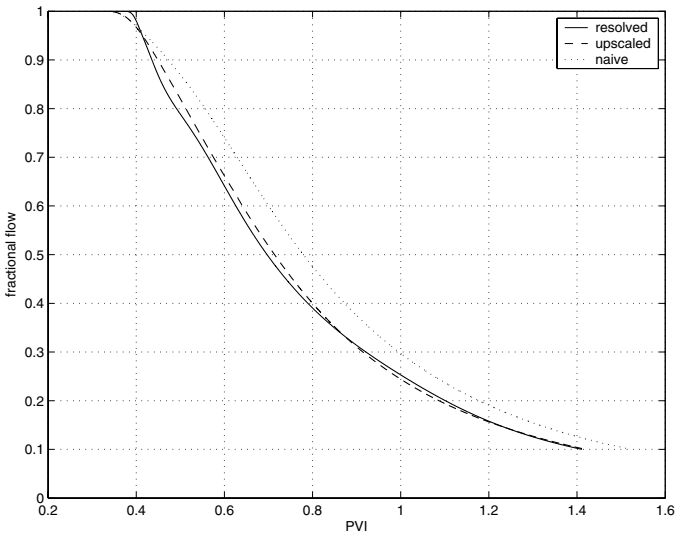

FIG. 13. *Comparison of the fractional flow curves for the single-phase case.*

far from the true fractional flow for all subsequent times. For the upscaled scheme, the fractional flow curve follows the true one closely at all times.

5.2.2. Two-phase results. For the two-phase flows we perform exactly the same analysis as was done above for the single-phase case. In this case, since it has already been demonstrated that MsFEM accurately captures the velocity field, we skip the comparisons of the velocity fields. For two-phase flow, there is not as much "fingering" of the saturation into the layers of high permeability as in the single-phase case, but there are still quite a lot of small-scale features. In Figure 14 we show the average saturations computed from the resolved computations and upscaled schemes

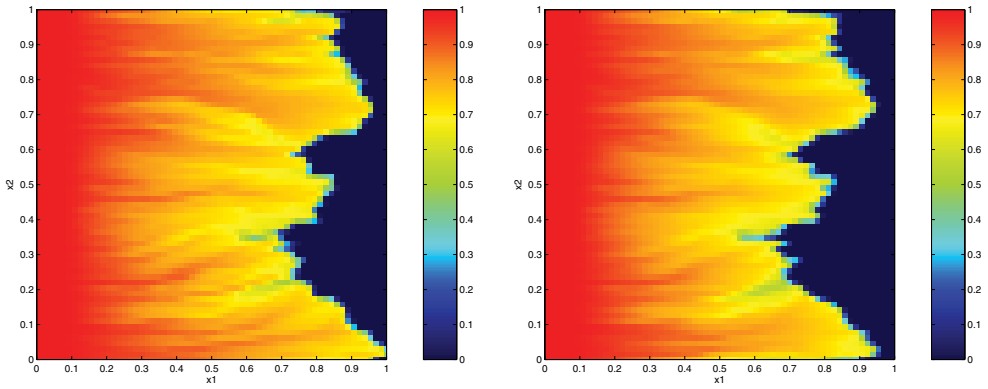

FIG. 14. *Comparison of the average saturation profiles for the two-phase case at* $t = 0.45$ *for the exact calculation (left) and upscaled scheme (right).*

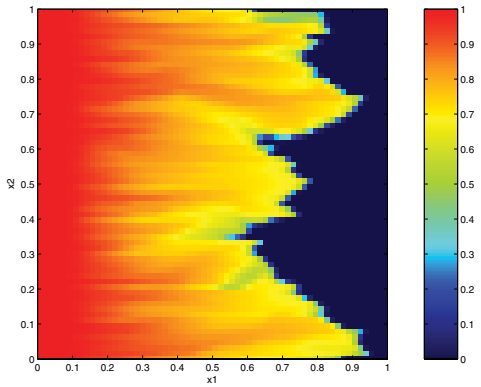

FIG. 15. *Average saturation profile at* $t = 0.45$ *for the naive method that ignores the subgrid interaction terms for the two-phase case.*

at time $t = 0.45$. One can see again that the upscaled method captures the average saturation accurately, while the naive method, which ignores the interaction term, does not move the average correctly, as shown in Figure 15. This is also evident from the fractional flow curves shown in Figure 16.

6. Concluding remarks. In this paper we have proposed a new framework for upscaling the hyperbolic saturation equation for the two-phase flow problem in porous media. In addition we have incorporated this into a numerical scheme for solving the full flow problem. The main goal of this work is to be able to solve the flow problem on coarse grids, because it is more computationally efficient and average (coarse grid) features are most often of engineering interest. The framework makes only limited assumptions on the nature of the small-scale features and is not as restrictive as previous methods. Through numerical examples we have demonstrated the ability of our method to accurately capture the average flow features. Further, our numerical method is extensible to the more realistic case where the small-scale features are nonperiodic.

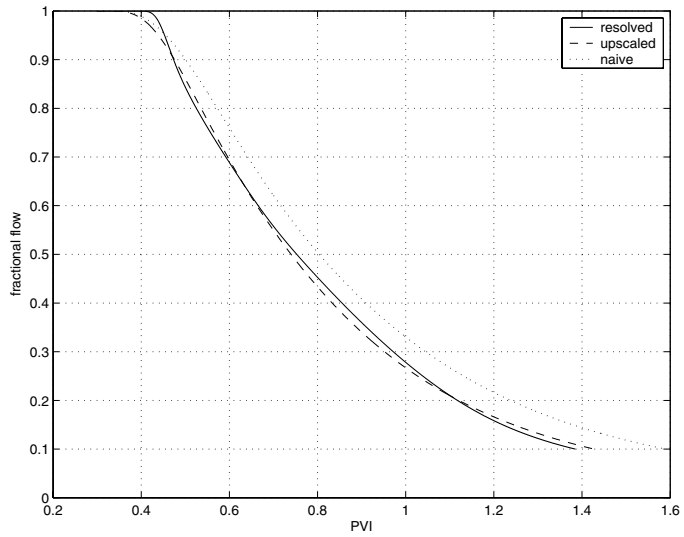

FIG. 16. *Comparison of the fractional flow curves for the two-phase case.*

REFERENCES

[1] R. BECKIE, A. A. ALDAMA, AND E. F. WOOD, *Modeling the large-scale dynamics of saturated groundwater flow using spatial filtering theory,* 1*, theoretical development*, Water Resour. Res., 32 (1996), pp. 1269–1280.

[2] A. BENSOUSSAN, J. LIONS, AND G. PAPANICOLAOU, *Asymptotic Analysis for Periodic Structures*, Stud. Math. Appl. 5, North–Holland, Amsterdam, 1978.

[3] D. BRAESS, *Finite Elements. Theory, Fast Solvers and Applications in Solid Mechanics*, Cambridge University Press, Cambridge, UK, 2001.

[4] S. E. BUCKLEY AND M. C. LEVERETT, *Mechanisms of fluid displacements in sands*, Trans. AIME, 146 (1942), pp. 107–116.

[5] H. CENICEROS AND T. Y. HOU, *An efficient dynamically adaptive mesh for potentially singular solutions*, J. Comput. Phys., 172 (2001), pp. 1–31.

[6] Y. CHEN, L. J. DURLOFSKY, M. GERRITSEN, AND X. H. WEN, *A coupled local-global upscaling approach for simulating flow in highly heterogeneous formations*, Adv. Water Resources, 26 (2003), pp. 1041–1060.

[7] Z. CHEN AND T. Y. HOU, *A mixed multiscale finite element method for elliptic problems with oscillating coefficients*, Math. Comp., 72 (2003), pp. 541–576.

[8] L. J. DURLOFSKY, *Numerical calculation of equivalent grid block permeability tensors for heterogeneous porous media*, Water Resour. Res., 27 (1991), pp. 699–708.

[9] W. E, *Linear and nonlinear transport equations*, Comm. Pure Appl. Math., 45 (1992), pp. 301–326.

[10] Y. EFENDIEV AND L. J. DURLOFSKY, *Numerical modeling of subgrid hetrogeneity in two phase flow simulations*, Water Resour. Res., 36 (2002), pp. 2031–2041.

[11] Y. EFENDIEV, L. J. DURLOFSKY, AND S. H. LEE, *Modeling of subgrid effects in coarse-scale simulations of transport in hetrogeneous porous media*, Water Resour. Res., 36 (2000), pp. 2031–2041.

[12] Y. EFENDIEV, V. GINTING, T. Y. HOU, AND R. EWING, *Accurate multiscale finite element method for two-phase flow simulations*, J. Comput. Phys., to appear.

[13] Y. R. EFENDIEV, *The Multiscale Finite Element Method and Its Applications*, Ph.D. thesis, California Institute of Technology, Pasadena, CA, 1999.

[14] Y. R. EFENDIEV, T. Y. HOU, AND X.-H. WU, *Convergence of a nonconforming multiscale finite element method*, SIAM J. Numer. Anal., 37 (2000), pp. 888–910.

[15] T. Y. HOU AND X. H. WU, *A multiscale finite element method for elliptic problems in composite materials and porous media*, J. Comput. Phys., 134 (1997), pp. 169–189.

[16] T. Y. HOU, X. H. WU, AND Z. CAI, *Convergence of a multiscale finite element method for*

elliptic problems with rapidly oscillating coefficients, Math. Comp., 68 (1999), pp. 913–943.
[17] T. Y. Hou and X. Xin, *Homogenization of linear transport equations with oscillatory vector fields*, SIAM J. Appl. Math., 52 (1992), pp. 34–45.
[18] T. Y. Hou, D. Yang, and H. Ran, *Multiscale analysis in the Lagrangian formulation for the 2-D incompressible Euler equation*, Discrete Contin. Dyn. Syst., 13 (2005), pp. 1153–1186.
[19] P. Jenny, S. Lee, and H. Tchelepi, *Multi-scale finite-volume method for elliptic problems in subsurface flow simulation*, J. Comput. Phys., 187 (2003), pp. 47–67.
[20] P. Jenny, S. H. Lee, and H. A. Tchelepi, *Adaptive multiscale finite-volume method for multiphase flow and transport in porous media*, Multiscale Model. Simul., 3 (2004), pp. 50–64.
[21] P. Langlo and M. Espedal, *Macrodispersion for two-phase, immiscible flow in porous media*, Adv. Water Resources, 17 (1994), pp. 297–316.
[22] R. LeVeque, *CLAWPACK* 4.1 *User's Guide* http://www.amath.washington.edu/∼claw/ (2002).
[23] R. LeVeque, *Finite-Volume Methods for Hyperbolic Problems*, Cambridge University Press, Cambridge, UK, 2002.
[24] J. G. Liu, *Homogenization and Numerical Methods for Hyperbolic Equations*, Ph.D. thesis, University of California, Los Angeles, CA, 1990.
[25] D. Peaceman, *Fundamentals of Numerical Reservoir Simulation*, Elsevier, Amsterdam, 1977.
[26] L. Tartar, *Nonlocal effects induced by homogenization*, in Partial Differential Equations and the Calculus of Variations, Birkhäuser, Boston, 1989, pp. 925–938.
[27] A. Westhead, *Upscaling for Two-Phase Flows in Porous Media*, Ph.D. thesis, California Institute of Technology, Pasadena, CA, 2005.
[28] K. Yosida, *Functional Analysis*, 6th ed., Springer-Verlag, Berlin, 1980.